Experimental Investigation on the Transport of Sulfide Driven by Melt-rock Reaction in Partially Molten Peridotite

Zhenjiang Wang[1], Zhuosen Yao[2], Zhenmin Jin[3], and Yannan Wang[4]

[1]Key Laboratory of Resource Exploration Research of Hebei Province, and School of Earth Science and Engineering, Hebei University of Engineering
[2]Department of Earth Sciences, Carleton University
[3]China University of Geosciences (Wuhan)
[4]Xinjiang Institute of Ecology and Geography Chinese Academy of Sciences

April 4, 2023

Abstract

Extraction of sulfides from the partially molten mantle is vital to elucidate the cycling of metal and sulfur elements between different geochemical circles but has not been investigated systematically. Using laboratory experiments and theoretical calculations, this study documents systematical variations in lithologies and compositions of silicate minerals and melts, which are approximately consistent with the results of the thermodynamically-constrained model. During a melt-peridotite reaction, the dissolution of olivine and precipitation of new orthopyroxene generate an orthopyroxene-rich layer between the melt source and peridotite. With increasing reaction degree, more melt is infiltrated into and reacts with upper peridotite, which potentially enhances the concomitant upward transport of dense sulfide droplets. Theoretical analyses suggest an energetically focused melt flow with a high velocity (~ 170.9 μm/h) around sulfide droplets through the pore throat. In this energic melt flow, we, for the first time, observed the mechanical coalescence of sulfide droplets, and the associated drag force was likely driving upward entrainment of fine μm-scale sulfide. For coarse sulfide droplets whose sizes are larger than the pore throat in the peridotite, their entrainment through narrow constrictions in crystal framework seems to be physically possible only when high-degree melt-peridotite reaction drives high porosity of peridotite and channelized melt flows with extremely high velocity. Hence, the melt-rock reaction could drive and enhance upward entrainment of μμ- το μμ-σϛαλε sulfide in the partially molten mantle, potentially contributing to the fertilization of the sub-continental lithospheric mantle and the endowment of metal-bearing sulfide for the formation of magmatic sulfide deposits.

[Journal of Geophysical Research: Solid Earth]

Supporting Information for

[Experimental Investigation on the Transport of Sulfide Driven by Melt-rock Reaction in Partially Molten Peridotite]

[Zhenjiang Wang[1,3], Zhuo-sen Yao[2], Zhenmin Jin[3], Yannan Wang[1]]

[[1]Key Laboratory of Resource Exploration Research of Hebei Province, and School of Earth Science and Engineering, Hebei University of Engineering, 056038 Handan, China.

[2]State Key Laboratory of Geological Processes and Mineral Resources, and School of Earth Resources, China University of Geosciences, 430074 Wuhan, China.

[3]State Key Laboratory of Geological Processes and Mineral Resources, and School of Earth Sciences, China University of Geosciences, 430074 Wuhan, China.

Corresponding author: Zhuo-sen Yao and Zhenmin Jin (yaozhuosen@cug.edu.cn; zmjin@cug.edu.cn)]

Contents of this file

Additional Supporting Information (Files uploaded separately)

Text S1. The methodology for the measurement of grain sizes of olivine and clinopyroxene

In this study, grain sizes of olivine and clinopyroxene in the partially molten peridotite were measured by mapping analyses of electron backscattered diffraction (EBSD) using a Quanta 450 FE-SEM equipped with an HKL Nordlys EBSD detector at the State Key Laboratory of Geological Processes and Mineral Resources (GPMR) of China University of Geosciences. Measurements were performed under the conditions of an accelerating voltage of ~ 20 kV, ~ 0.8 μm step size, a beam current of ~ 6 nA, a tilt angle of ~ 70°, and about ~ 20-25 mm working distance. The smallest detectable grain size was about ~ 4 μm. EBSD patterns of different crystal minerals are determined by the orientations of the grains being examined. By scanning the beam in a grid pattern, a map of the grain orientations can be produced. When a discontinuous change in the orientation occurs, this indicates that a grain boundary has been crossed. The misorientations of greater than 15° were recorded as being distinct grains. Then, orientation maps of different crystal minerals can be built using the commercially available software channel5© to obtain grain sizes of different minerals.

Text S2. The methodology for the measurement of water content in silicate melt using Fourier transform infrared spectroscopy (FTIR)

We used the FTIR to determine the water content of silicate melt in experiments PC520 and PC528 at the State Key Laboratory of Geological Processes and Mineral Resources (GPMR) of China University of Geosciences. Before the FTIR measurements, the samples were double polished to a thickness of 100 μm and kept in a vacuum stove at 400 K for at least 12h to preclude the grain boundary water in samples. The water content can be calculated by using the Beer-Lambert law:

$$C_H = \frac{A \times 18.0152}{d \times \rho \times \varepsilon}, \quad (1)$$

where C_H is the total H_2O content (wt.%), A is the measured absorbance of the peak at 3550 cm^{-1}, after linear baseline correction (≤1), d is the sample thickness (cm); ρ is the density (g L^{-1}) of silicate melt, ε is the molar absorptivity (62.8 ± 0.8 L mol^{-1} cm^{-1}) (Mercier et al., 2010).

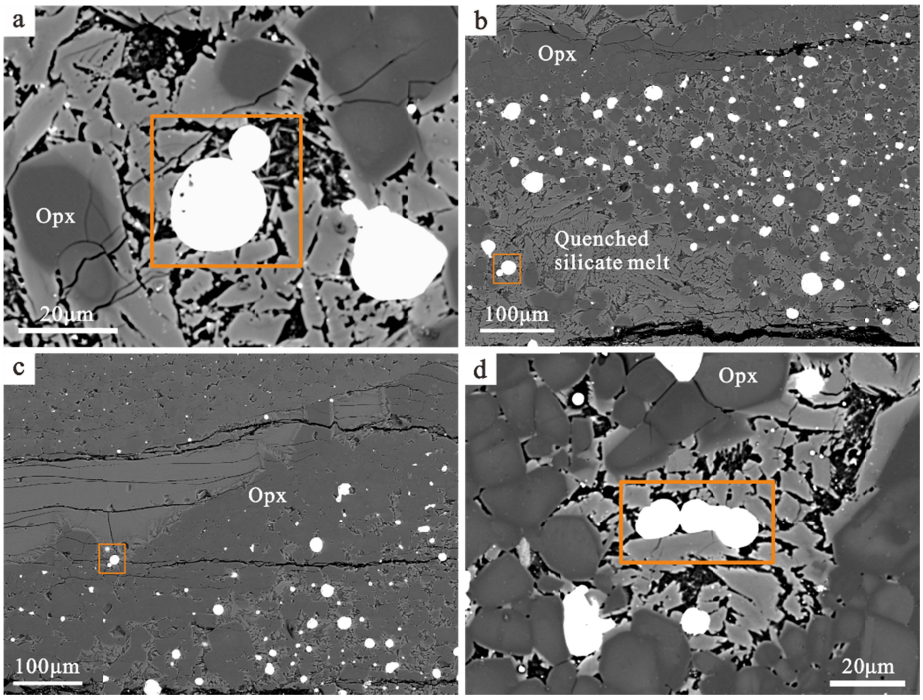

Figure S1. Microstructures of two sulfide droplets contacting each other from experiments PC527 (a-b), PC528 (c), and PC545 (d). Yellow squares denote that two sulfide droplets are contacting and coalescing with each other. Opx-orthopyroxene.

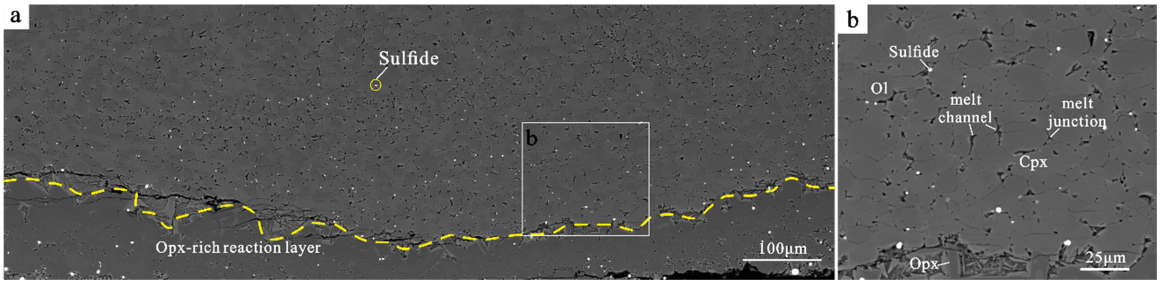

Figure S2. Microstructures of the peridotite and the Opx-rich reaction layer from experiment PC520 (~ 1.5 GPa, ~ 1,250 ℃, ~ 12h). The dashed yellow line denotes the top of the Opx-rich reaction layer. The bright white spots in the peridotite are sulfide droplets entrained by the reactive melt flow from the lower melt source. Melt junctions and channels are also designated in (b). Ol-olivine; Opx-orthopyroxene; Cpx-clinopyroxene.

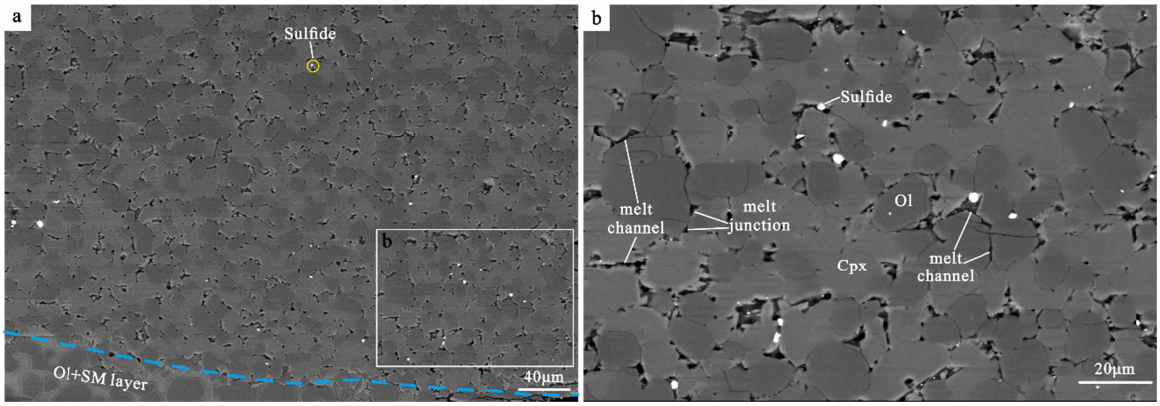

Figure S3. Microstructures of the peridotite and the olivine-melt layer (the Ol+SM layer) from experiment PC527 (~ 1.5 GPa, ~ 1,300 °C, ~ 12h). The dashed cyan line denotes the top of the olivine-melt layer. Symbols are the same as in Figure S2. Ol-olivine; Cpx-clinopyroxene; SM-silicate melt.

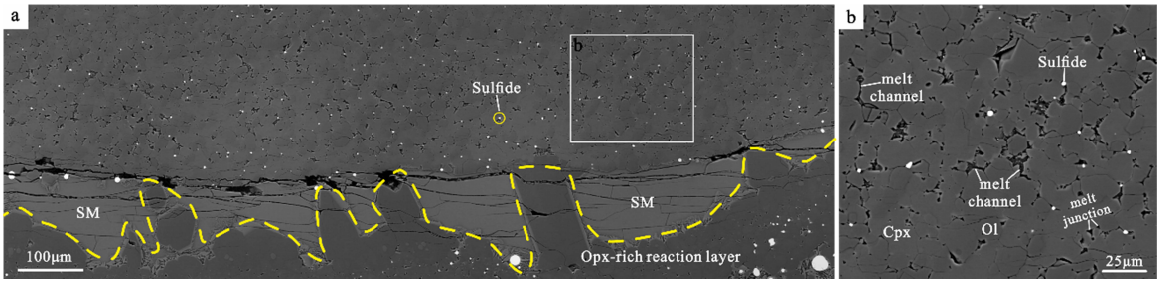

Figure S4. Microstructures of the peridotite and the Opx-rich reaction layer from experiment PC528 (~ 1.5 GPa, ~ 1,250 °C, ~ 48h). Symbols are the same as in Figure S2. Ol-olivine; Cpx-clinopyroxene; Opx-orthopyroxene; SM-silicate melt.

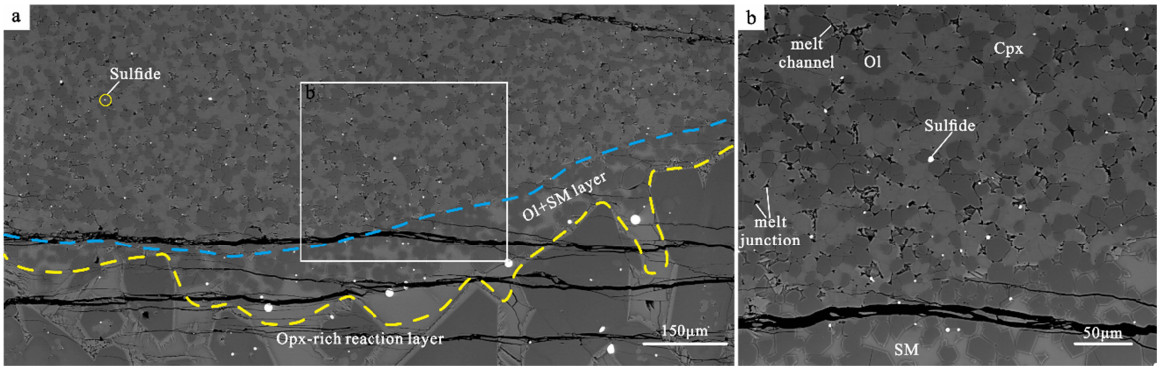

Figure S5. Microstructures of the peridotite, the olivine-melt layer, and the Opx-rich reaction layer from experiment PC545 (~ 1.5 GPa, ~ 1,250 °C, ~ 72h). The dashed blue and yellow lines denote the tops of the olivine-melt layer and Opx-rich reaction layer, respectively. Symbols are the same as in Figure S2. Ol-olivine; Opx-orthopyroxene; Cpx-clinopyroxene; SM-silicate melt.

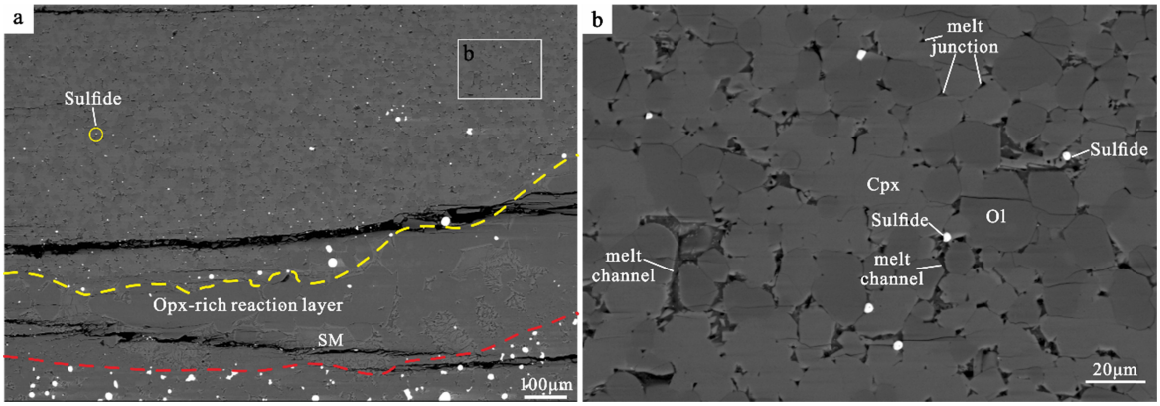

107

112 **Figure S6.** Microstructures of the peridotite and the Opx-rich reaction layer from experiment
113 PC548 (~ 1.5 GPa, ~ 1,250 ℃, ~ 48h). The dashed yellow and red lines denote the top of the
114 Opx-rich reaction layer and the original interface between the melt source and peridotite before
115 the melt-rock reaction, respectively. Symbols are the same as in Figure S2. Ol-olivine; Opx-
116 orthopyroxene; Cpx-clinopyroxene; SM-silicate melt.

113

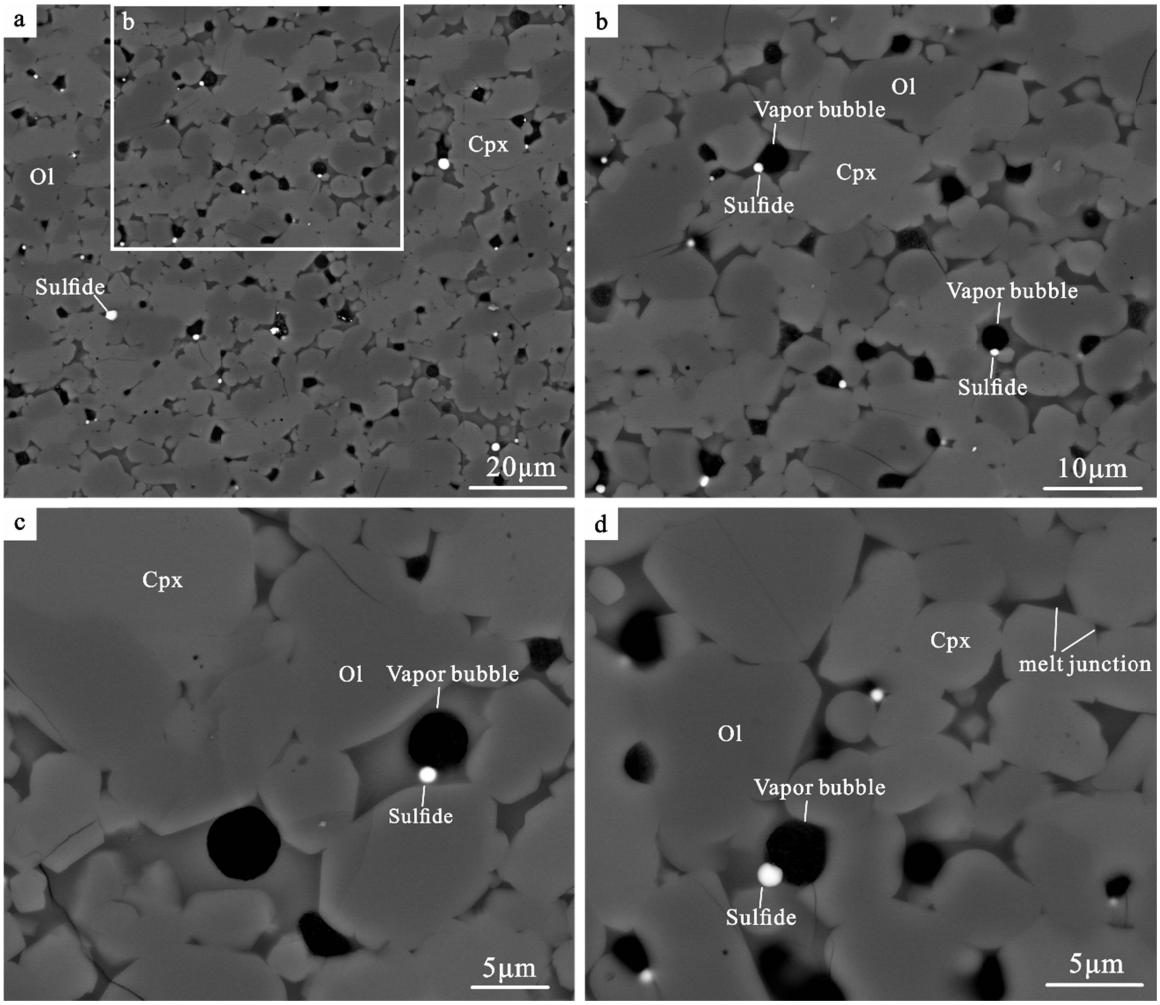

114

Figure S7. Microstructures of the partially molten peridotite from experiment PC559 (~ 0.5 GPa, ~ 1,200 ℃, ~ 6h). The low pressure (~ 0.5 GPa) potentially leads to the presence of vapor bubbles (mainly H_2O) in the peridotite, forming some sulfide-vapor aggregates. Symbols are the same as in Figure S2. Ol-olivine; Cpx-clinopyroxene.

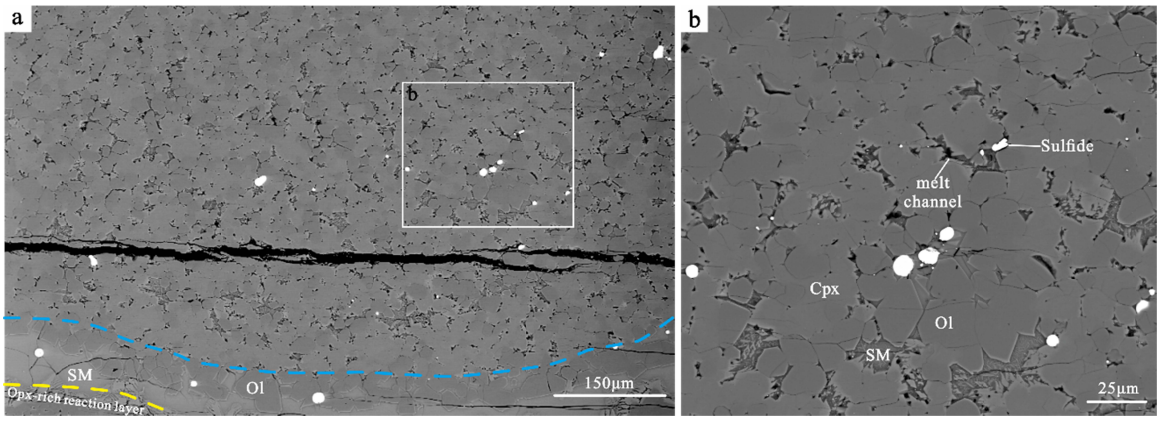

Figure S8. Microstructures of the peridotite, the olivine-melt layer, and the Opx-rich reaction layer from experiment PC560 (~ 1.5 GPa, ~ 1,250 ℃, ~ 24h). Symbols are the same as in Figure S5. Ol-olivine; Opx-orthopyroxene; Cpx-clinopyroxene; SM-silicate melt.

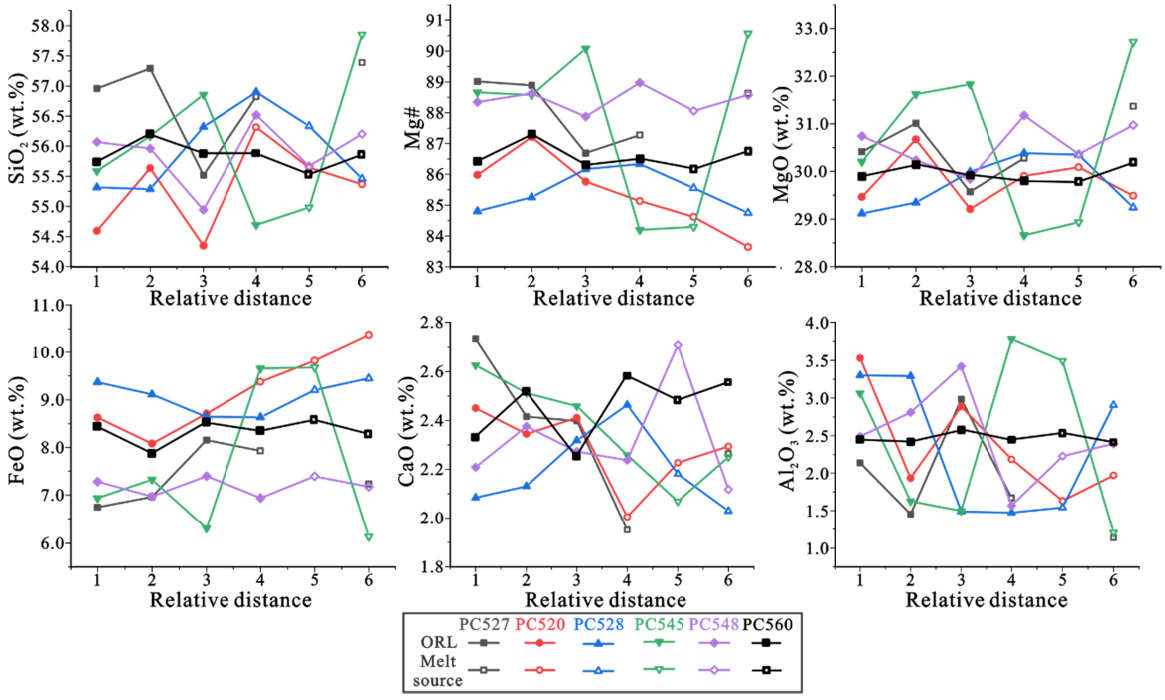

Figure S9. Plots of analyzed oxide abundance (in wt.%) and Mg# of orthopyroxene grains from the ORL to the melt source. The relative distance "1" represents the top of the ORL. The analyzed points are about 50-150 μm apart, depending on the size of orthopyroxene grains and the thickness of ORL.

Table S1. The statistical results of grain sizes of olivine and clinopyroxene in the upper partially molten peridotite of run PC520, PC528, and PC545.

Table S2. The statistical results of grain size of sulfide droplets in these experiments of this study.

Table S3. The composition of starting materials.

Table S4. EPMA data of olivine, Cpx, and Opx for Figures 6-7.

Table S5. EPMA data of silicate melt and sulfides for Figure 8.

Table S6. The results of the thermodynamically-constrained model for Figures 6-8.

Experimental Investigation on the Transport of Sulfide Driven by Melt-rock Reaction in Partially Molten Peridotite

Zhenjiang Wang[1,3], Zhuo-sen Yao[2], Zhenmin Jin[3], Yannan Wang[1]

[1]Key Laboratory of Resource Exploration Research of Hebei Province, and School of Earth Science and Engineering, Hebei University of Engineering, 056038 Handan, China.

[2]State Key Laboratory of Geological Processes and Mineral Resources, and School of Earth Resources, China University of Geosciences, 430074 Wuhan, China.

[3]State Key Laboratory of Geological Processes and Mineral Resources, and School of Earth Sciences, China University of Geosciences, 430074 Wuhan, China.

Corresponding author: Zhuo-sen Yao and Zhenmin Jin (yaozhuosen@cug.edu.cn; zmjin@cug.edu.cn)

Key Points:

- Systematical variations are produced by the melt-rock reaction in lithologies and compositions of silicate melt and minerals
- Melt-rock reaction is conducive to the upward transport of sulfide droplets in a crystal framework based on experimental observation
- Focused melt flow with high velocity can drive upward extrusion and entrainment of μm- to mm-scale sulfides through narrow melt tubes

Abstract

Extraction of sulfides from the partially molten mantle is vital to elucidate the cycling of metal and sulfur elements between different geochemical circles but has not been investigated systematically. Using laboratory experiments and theoretical calculations, this study documents systematical variations in lithologies and compositions of silicate minerals and melts, which are approximately consistent with the results of the thermodynamically-constrained model. During a melt-peridotite reaction, the dissolution of olivine and precipitation of new orthopyroxene generate an orthopyroxene-rich layer between the melt source and peridotite. With increasing reaction degree, more melt is infiltrated into and reacts with upper peridotite, which potentially enhances the concomitant upward transport of dense sulfide droplets. Theoretical analyses suggest an energetically focused melt flow with a high velocity (~ 170.9 μm/h) around sulfide droplets through the pore throat. In this energic melt flow, we, for the first time, observed the mechanical coalescence of sulfide droplets, and the associated drag force was likely driving upward entrainment of fine μm-scale sulfide. For coarse sulfide droplets whose sizes are larger than the pore throat in the peridotite, their entrainment through narrow constrictions in crystal framework seems to be physically possible only when high-degree melt-peridotite reaction drives high porosity of peridotite and channelized melt flows with extremely high velocity. Hence, the melt-rock reaction could drive and enhance upward entrainment of μm- to mm-scale sulfide in the partially molten mantle, potentially contributing to the fertilization of the sub-continental lithospheric mantle and the endowment of metal-bearing sulfide for the formation of magmatic sulfide deposits.

Plain Language Summary

Sulfides are a pivotal potential reservoir for sulfur and economically important metals. Their transport in the Earth's mantle plays a vital role in understanding many crucial geological and environmental processes, especially the formation of mineral deposits, and the environmental damage and health hazards related to volcanic eruptions. This work proposes a new driving force for the upward transport of dense sulfide drops in the upper mantle that experiences partial melting. The reaction between melt and rock potentially leads to focused melt flow in new-forming channels with three orders of magnitude higher velocity than that of melt flowing among the crystal framework of peridotite. This energetic melt flow drives the upward transport of tiny

μm-scale sulfide droplets in peridotite and may also facilitate the amalgamation of droplets contacting each other. Coarse sulfide droplets could be possibly entrained upward through narrow pore throats, especially when a high-degree melt-peridotite reaction drives fast-flowing melt in the mantle with high porosity.

1 Introduction

Sulfide is a ubiquitous phase in the mantle (Alard et al., 2011) and an important repository for sulfur and geochemically and economically important chalcophile metals, which plays a pivotal role in the partitioning behaviors of PGE, Cu, and Ni (Mungall & Brenan, 2014; Patten et al., 2013). Understanding the factors that control the fate of sulfide phases in the partially molten mantle is of fundamental importance in exploring the recycling of sulfur and chalcophile elements among different geochemical reservoirs (Ding & Dasgupta, 2017; Farquhar et al., 2002; Yao et al., 2018; Chen et al., 2022) and identifying the re-fertilization of the depleted lithospheric mantle, which potentially provides the metal endowment for the formation of Cu-rich porphyry and/or Ni-rich magmatic ore system (Holwell et al., 2022; Lee & Tang, 2020; Mungall et al., 2015; Zhao et al., 2022). However, it remains highly contentious for the driving forces of the transport of metal-bearing sulfide liquid, which severely blocks our understanding of the details of fertilization processes that occurred in the sources of sulfide-related magmatic and hydrothermal deposits.

Conventionally, the removal of sulfide from a partially molten peridotite requires progressive dissolution of sulfide into the departing silicate melt (Holzheid & Grove, 2002; Mungall & Brenan, 2014; Yao et al., 2018). Nevertheless, the mechanical entrainment of sulfide could also potentially be an efficient process driving the redistribution and local enrichment of sulfur and chalcophile elements in the mantle (Iacono-Marziano et al., 2022; Heinrich & Connolly, 2022; Z. Wang et al., 2020; Yao & Mungall, 2020). Although a small amount (< percolation thresholds) of sulfide under hydrostatic conditions may not be entrained through the slow porous flow of silicate melt due to high surface tension (Bagdassarov et al., 2009; Holzheid et al., 2000; Yoshino et al., 2003, 2004), it has been argued that the extraction of sulfide driven by stress in a partially molten peridotite could be further facilitated by the directional porous flow of silicate melt, strongly affecting the fractionation and abundances of chalcophile metals in the mantle melting products, *i.e.*, basalts (Ballhaus et al., 2006; Bockrath et al., 2004; Z. Wang et

al., 2020). Except for the deviatoric stress, a preliminary experimental study (Wang & Jin, 2020) proposed that during the melt-rock reaction, entrainment of sulfide liquid may be enhanced by the reaction infiltration instability (RII) in the partially molten peridotite when a reacting melt percolates through a dissolvable, porous, melt-mineral mixture. The mechanical transport and enrichment of sulfide during this melt-rock reaction have been extensively demonstrated in mantle peridotites, which has clarified some geochemical paradoxes of the chalcophile/siderophile elements (Ciazela et al., 2018; Lorand & Luguet, 2016). The RII theory proposed by Chadam et al. (1986) also applies to magmatic systems by introducing compaction of crystal mush and driving a solubility gradient along the flow direction instead of the propagating reaction front (Aharonov, 1995), resulting in positive feedback among the increasing permeability driven by melt-rock reaction and the associated reinforcement of melt flux in reacting regions. This melt-rock reaction is well known as a pervasive process even forming melt-rich channels with an extremely speedy magma flow due to the positive feedback in partially molten regions of the mantle, which has been broadly demonstrated by geological investigations (*e.g.*, Kelemen et al., 1995; Sundberg et al., 2010), high-temperature, high-pressure (HTHP) laboratory works (*e.g.*, Daines & Kohlstedt, 1994; Pec et al., 2015) and theoretical analyses (Aharonov, 1995; Chadam et al., 1986; Spiegelman et al., 2001). During a reaction of melt with a depleted mantle, melt re-fertilization processes potentially occur, thereby impregnating the mantle with sulfides, which have been widely found in mantle xenoliths, orogenic and abyssal peridotites (*e.g.*, Ciazela et al., 2018; Luguet et al., 2003; Niu, 2004; Wang et al., 2009).

Although it has been tentatively demonstrated that the rapid enough ascending magma flow in these melt-rich channels could hold upward entrainment of large olivine phenocrysts or even dense sulfide droplets during a melt-rock reaction (Pec et al., 2017; Wang & Jin, 2020), extraction of sulfide driven by the RII has received little attention, and the precise physical and chemical constraints about these processes appear to be worth studying thoroughly. Here we conducted systematically two-layer reaction experimental studies in which a partially molten peridotite was placed on a sulfide-bearing silicate melt source to explore the entrainment of sulfide liquids driven by the RII and trace the physical and chemical variations of liquid and solid phases during these processes, which sheds lights on the fertilization of lithospheric mantle, as well as the formations of magmatic and/or hydrothermal sulfide deposits.

2 Experimental Methods

2.1 Starting materials

As a melt source, the starting materials were a mixture of the powdered calc-alkaline tholeiitic basalt (70 wt.%) from the East Pacific Rise (102.7044 °W, 2.64961 °S), olivine crystals (20 wt.%) from fresh spinel lherzolite xenoliths at Damaping (Hannuoba region, North China), and sulfide aggregates (10 wt.%) from Jinchuan Ni-Cu sulfide deposit, NW China. Additionally, 0 or 2 wt.% oceanic sediments (mainly carbonate) were mixed into the melt source. The sulfide aggregate (59 wt.% pyrrhotite, 36 wt.% pentlandite, and 5 wt.% chalcopyrite) adopted here is similar to that in massif peridotites (Lorand et al., 2010), and was grounded in alcohol for about 6h to < 10 μm measured by using the scanning electron microscope (SEM).

To prepare a partially molten rock, the olivine and clinopyroxene crystals from Damaping spinel lherzolite xenoliths were mixed in a 50:50 ratio by weight. Then, ~ 0 or ~ 5 wt.% calc-alkaline tholeiitic basalt was added to change the initial porosity of the crystal framework. All silicate mineral grains were ground to about 10-20 μm grain size in an agate mortar. The partially molten rock was placed on the melt source to explore the possible upward transport of dense sulfides from the melt source to the peridotite. The length ratio of these two parts was slightly larger than ~ 1:1 to avoid chemical equilibration among them over the experimental time scales. Compositions of these starting materials were described by Z. Wang et al. (2020) (Table S3), and Table 1 lists the experimental conditions.

2.2 Experimental methods and analytical techniques

The two-layer reaction experiments were conducted via a 150 Ton non-end-loaded type piston-cylinder press at China University of Geosciences. Starting materials mentioned above are loaded into a cylindrical platinum (Pt) capsule (3.75 mm diameter; 5-6 mm high) with a graphite inner sleeve (Figure 1-inset in the lower left). Due to the graphite inner sleeve, the oxygen fugacity of this experimental system was maintained at about CCO-0.8 (the graphite-CO_2 buffer), which corresponds to a log fO_2 < FMQ-2 log unit at ~ 1,360 ℃ and 1.5 GPa (*e.g.*, Médard et al., 2008). Information on experimental assembly can be found in our previous work (Z. Wang et al. 2020). In order to remove absorbed water, a 12-hour heating (120 °C) in a vacuum oven is conducted for all capsules before being sealed, and we did not observe any

apparent sulfur loss during this drying. The experiment conditions in Table 1 should be held for 12-72 h, and then these materials were quenched to room temperature.

Polished sections were prepared from the recovered experimental specimens cut parallel to the specimen axis. The observation of microstructure in these sections was conducted via a Quanta 450 field-emission scanning electron microscope (FE-SEM) at China University of Geosciences, with a 6.0 μm spot size, 20 kV accelerating voltage, and 12 mm working distance. The backscattered electron (BSE) images were adopted to measure the morphological characteristics of experimental products, such as the dissolution distance, the thickness of reactive boundary layers, and the size of sulfide droplets. Quantitative compositional analyses for olivine and clinopyroxene were obtained via a JEOL JXA-8230 electron probe microanalyzer with four wavelength-dispersive spectrometers (WDS) at China University of Geosciences, with an accelerating voltage of 15 kV, a probe current of 20 nA and a beam diameter of 1 μm. Sulfides were analyzed with a higher accelerating voltage (20 kV), and the compositions of quenched silicate melts were measured with a smaller probe current (10 nA). A defocused beam of 20-30 μm diameter was adopted here for all the standardizations, quenched melts, and sulfides. Dwell times were 10s on element peaks and half that on background locations adjacent to peaks. Raw X-ray intensities were corrected using a ZAF (atomic number, absorption, fluorescence) correction procedure. A series of natural and synthetic SPI standards were utilized and changed based on the analyzing minerals. The following standards were used: sanidine (for K), pyrope garnet (for Al), almandine garnet (for Fe), diopside (for Ca, Si, Mg), jadeite (for Na), rhodonite (for Mn), olivine (for Si, Mg), rutile (for Ti), apatite (for P), chromium oxide (for Cr). The analytical standards for sulfides were pentlandite (for Fe, Ni, S) and native copper (for Cu) (Pan et al., 2023).

3 Results

In order to investigate the physical migration of sulfide during reaction infiltration of silicate melt in the partially molten mantle, we have conducted eight reaction experiments at 0.5-1.5 GPa, 800-1,300 ℃, and 12-72 h (Table 1). Generally, several distinct lithological regions were developed and, from bottom to top, respectively separated by a diffuse-dominated, mineralogical interface in these two-layer reaction experiments (Figure 1; Figures S2-S8). The

freeware ImageJ (http://imagej.nih.gov/ij/) from the National Institute of Health was adopted to analyze all two-dimensional BSE images obtained here.

3.1 Phase assemblages and textures

Under the low-temperature, high-pressure conditions (800 ℃ and 1.5 GPa), both minerals and sulfides were generally polygonal and not molten, and sulfide droplets in the lower part of the sample were uniformly distributed in pores among silicate grains. At 1.5 GPa, when the experimental temperatures exceed ~1,250 ℃, the basaltic material was completely molten, and the diameter of sulfide droplets ranges from several μm to > 100 μm (Figure 1). Gravitational segregation of sulfide was insignificantly observed in all sections, but obviously, some huge sulfide droplets were attached to the wall of the graphite capsule, especially at high temperature and long experiment durations (Figure 1). These coarse droplets were excluded from the collected data to calculate the average sulfide size. Tiny exsolution lamellae with higher backscattered electron (BSE) intensity were occasionally observed in some quenched large sulfide droplets. Sometimes silicate melts were pooled at the edge of the sample (Figure 1).

In all high-pressure experiments (1.5 GPa), an orthopyroxene (Opx)-rich reaction layer (ORL) was formed at the boundary of the lower melt source and upper partially molten peridotite due to the reaction between them, and chiefly composed of Opx grains, silicate melt, and sulfide droplets (Figure 1). With increasing the annealing time and/or run temperature, the morphology of ORLs became more irregular (Figure 1b; Figures 2a, b, and d), and small olivine inclusions were observed in a few large Opx grains (Figure 2a). The ORL at 1,300℃ was even ruptured mainly due to the growth of several Opx grains to enormous size (> 100 μm) and possible gravitational settling (Figure 2d). We also observed the bulge of ORL toward the melt source (Figure 1b), which can be attributed to the slight gravitational settling of Opx and volumetric shrinkage of the melt source after the upward reactive percolation of silicate melt. Thus, the original interface between the melt source and peridotite before the experimental reaction cannot be marked by the offset of the graphite inner sleeve. At 1,250 ℃, the thickness of ORL increases from ~ 118 ± 11 μm (1σ) at 12 h to ~ 416 ± 119 μm at 72 h, which is likely a linear function of the square root of the run duration (slope = 0.78 ± 0.05) (Figure 3a-blue line). With increasing the temperature to 1,300 ℃, the thickness increases considerably to 500 ± 128 μm at 12 h (Figure 3a), implying the contribution of a higher temperature to the growth of ORL.

Additionally, based on the linear fit, the addition of 5 wt.% basalts into the partially molten peridotite (run PC548) or 2 wt.% oceanic sedimentary into the melt source (run PC560) seems to have no significant effect on the thickness of ORL (Figure 3a).

On the other hand, peridotites in the upper part of our samples were in disequilibrium with silicate melt at these run conditions, thereby should be dissolved essentially into the melt. The degree of dissolution is indirectly quantified via the dissolution distance (Figure 3b), which is the distance between the current boundary (Figure 1-blue dotted lines) and the original interface (Figure 1-red dotted lines) that is approximately represented by a sharp decrease in the size of sulfide droplets in the melt source. All these dissolution distances are measured at least 5 times around the central part of experimental charges. Similarly, dissolution distance linearly increases with the square root of time (Figure 3b-blue line) at 1,250 °C, and the increase of temperature to 1,300 °C significantly enlarges the dissolution distance (Figure 3b). The addition of oceanic sedimentary (PC560) or basalt (PC548) has no substantial effect on the dissolution distance (Figure 3b).

Moreover, based on analyses of SEM images, with increasing run duration or temperature, more silicate melt penetrated the Opx reaction layer into the partially molten peridotite (~ 4.65 ± 0.78 area% at 12 h; ~ 7.13 ± 0.58 area% at 72 h) (Figure 4a), resulting in the formations of melt junctions and channels among silicate minerals, and even some large melt pools just above the ORL (Figure 2c; Figures S2-S8). At 1.5 GPa, with increasing annealing time from 12 h to 72 h, the grain size of silicate minerals increases from 8.1 ± 3.4 μm to 11.0 ± 4.9 μm in the partially molten peridotite (Figure 4b; Supporting information; Table S1). Under conditions of high temperature (1,300 °C) and long-run duration (72 h), an olivine-melt layer, consisting of sulfide, olivine, and silicate melt, is present above the ORL (Figures 2a and 2d, Figures S3 and S5), which may be attributed to the dissolution of clinopyroxene and reprecipitation of olivine during the melt-peridotite reaction. Additionally, crystal faces between olivine grains were open and full of silicate melt, forming abundant melt channels among the crystal framework (Figure 2c, Figures S2-S8).

In the melt source, an amount of Opx grains were produced by the reaction between olivine in starting materials and convecting silicate melt (Figure 1), and there is commonly no significant boundary between these Opx grains and the ORL. The mean area-weighted diameter

of sulfide droplets was ~ 4.1 ± 0.1 μm in a low-temperature hot-press experiment (PC537, 800 °C), which potentially denotes the initial size of sulfide droplets in the starting material. At a higher temperature (1,250 °C), sulfide size increases from ~ 14.7 ± 0.2 μm to ~ 49.4 ± 1.6 μm with increasing the annealing time from 12 h to 72 h (Figure 5a; Table S2), in which the larger standard deviations from the long annealing time (72 h) experiments may be partly attributed to the presence of some enormous (> 50 μm) and tiny (< 1 μm) sulfide droplets. Under the same annealing time (48 h), there is no conspicuous increase in sulfide size when 5 wt.% basalt was added to the peridotite (PC548), but a slight increase in sulfide size was observed if the experimental temperature increased to 1,300 °C (PC527) (Figure 5a). The addition of carbonate into the melt source (PC560) resulted in a significant increase in sulfide size to ~ 54.0 ± 1.6 μm at 24 h (Figure 5a). Additionally, we also observed that the number density of sulfide droplets uniformly decreases with increasing annealing time in the lower melt source (Figure 5a-inset). The area fraction of sulfide in the melt source of the low-temperature experiment (800 °C) was ~ 3.26 ± 0.12 area%. At 1,250 °C, the area fraction was essentially constant (3.44 ± 0.14 area% at 12h; 3.50 ± 0.15 area% at 48h) when the annealing time was less than 48 h, but a visible increase (5.46 ± 0.22 area%) can be observed for a longer annealing time, 72 h (Figure 5b). A similar trend was also shown in the upper part of samples (Figures 5c and 5d), which may be due to more silicate melts infiltrating into the upper part of samples with increasing annealing time to 72 h (Figure 4). As previously observed (Yoshino & Watson, 2005), the diffusion of Fe and Ni components from silicate phases into sulfide liquids may be one of the reasons for the increase of sulfide area fraction in the melt source. In contrast, with increasing temperature to 1,300 °C, a lower area fraction (2.93 ± 0.07 area %) of sulfide was observed even in the experiment with a short annealing time (12 h) (Figure 5b), potentially due to partial dissolution of sulfide driven by the higher sulfur content at sulfide saturation (SCSS) at high temperature (*e.g.*, Liu et al., 2007; Mavrogenes & O'Neill, 1999). Similarly, the additions of basalt and carbonate enhance the permeation of more silicate melt into the upper part of samples, thereby increasing the area fraction of sulfide in the melt source (Figure 5b).

Based on the SEM images of products from these high-temperature experiments (1,250 °C), it becomes evident that sulfide droplets in the melt source were entrained into the partially molten peridotite by a porous flow of silicate melt during the melt-peridotite reaction (Figure 2). With permeating more silicate melt upwards, more and larger sulfide droplets can be observed in

the partially molten peridotite, and meanwhile their sizes (area-weighted diameter ~ 3.1 ± 0.1 μm at 12 h to ~ 11.1 ± 0.4 μm at 72 h) and area fractions (~ 0.15 ± 0.05 area% at 12 h to ~ 0.49 ± 0.03 area% at 72 h) increase with the increasing annealing time at 1,250 °C (Figures 5c and 5d; Table S2). Apparently, the addition of carbonate and 5 wt.% basalt into melt source and partially molten peridotite, respectively, drives a higher area fraction and larger size of sulfide droplet in the upper part of samples (Figures 5c and 5d). Hence, these observations propose that the ORL may not efficiently prevents the upward transport of silicate melt and sulfide droplets from the lower melt source to the upper molten peridotite.

Notably, under the condition of lower pressure (0.5 GPa), some vapor bubbles have been found in the partially molten peridotite due to the exsolution of volatile (mainly H_2O) in the starting basaltic material, and they mostly absorb on sulfide droplets to form compound drops, which has been proposed to potentially enhance the upward transport of sulfide (Figure S7; Mungall et al., 2015; Yao & Mungall, 2020).

3.2 Phase compositions

3.2.1 Mineral compositions

Figure 6 and Figure 7 respectively showed the compositional variations of olivine and clinopyroxene as a function of distance away from the final melt-peridotite interface (Table S4). At 1.5 GPa and 1,250-1,300 °C, from the far-field region to the interface, olivine grains became gradually lower in the Mg# (defined as molar Mg/(Mg+Fe)*100) and concentrations of SiO_2, MgO, and NiO, and meanwhile shown the increases in the FeO and MnO contents (Figure 6). Compared with the low-temperature, hot-press experiment (PC537) (Figure 6 purple dotted lines), olivine grains from high-temperature experiments contain lower MgO and NiO, and higher FeO and CaO concentrations. By contrast, olivine compositions in experiments PC548 (5 wt.% basalts) and PC559 (0.5 GPa) were roughly constant across the partially molten peridotite, whereas olivine grains crystallized in the melt source at lower-pressure experiment (0.5 GPa, PC559) had lower Mg#, MgO, SiO_2 and higher FeO than those in the peridotite region (Figure 6).

In contrast to olivine, more scatter compositions were observed in the clinopyroxene (Cpx) grains from the partially molten peridotite (Figure 7). Only near the melt-rock interface,

289 the trends of decreasing Mg# and CaO and increasing FeO were present in Cpx grains from all
290 high-pressure experiments, whereas the Cpx compositions in the low-pressure and carbonate-
291 bearing experiment (PC559 and PC560) were essentially constant across the peridotite region
292 (Figure 7). On the other hand, the Opx grains in the reaction layer and melt source were the
293 products of silicate melt-olivine reaction. No distinct compositional difference was observed in
294 these Opx grains (Figure S9; Table S4).

295 3.2.2 Silicate melt and sulfide liquid compositions

296 The variations of the reacted melt compositions in these experiments mostly depend on
297 the extent of the melt-rock reaction and the formation of a new major phase. In the melt source,
298 with increasing run time and/or temperature, the compositions of silicate melt became higher in
299 CaO and MgO concentrations, and lower in SiO_2, Al_2O_3, and FeO (Figure 8; Table S5), implying
300 the effect of high-degree melt-peridotite reaction on the melt composition. No distinct variation
301 of the melt sulfur contents was observed under the conditions of 1,250 ℃ and 1.5 GPa. Based on
302 two new SCSS models (Chowdhury and Dasgupta, 2020; Smythe et al., 2017), the calculated
303 ranges of SCSS in silicate melt are almost the same or slightly lower than our results within the
304 error of measurement (Figure 8f-shadow gray region), potentially indicative of sulfur-saturated
305 silicate melt in these experiments. Moreover, the calculated SCSS in the melt source is nearly the
306 same as those in the interface within the error, which is consistent with our measurements
307 (Figure 8f). The decreases in pressure and temperature respectively to 0.5 GPa and 1,200 ℃
308 caused the obvious increases in SiO_2 and Al_2O_3 concentrations and decreases in MgO and S
309 concentrations in silicate melt (Figures 8a, 8b, 8e, and 8f). No significant variations of melt
310 compositions were observed between the melt source and melt-peridotite interface within the
311 error of measurement (Figure 8), suggesting the convective flow is strong enough to drive the
312 chemical equilibrium of silicate melt. The composition of primary silicate melt infiltrating into
313 the peridotite cannot be analyzed due to the small scale. In addition, ~ 1.57 ± 0.15 wt.% H_2O was
314 detected in the reacted melts from experiments PC520 and PC528 using the Fourier Transform
315 Infrared Microscopy (Supporting Information, Mercier et al., 2010), which is slightly higher than
316 that of basalt (~ 1.19 wt.%) added in the starting materials. On the basis of these melt
317 compositions, the viscosity (μ_m) of the starting basalt (~ 1.19 wt.% H_2O) before the melt-rock
318 reaction can be calculated as ~ 10.8 Pa·s at 1.5 GPa and 1,250 ℃ by using the model from
319 Giordano et al. (2008), whereas the μ_m of reacting melt after the reaction decreases to ~ 1.2-2.7

Pa·s at 1.5 GPa and 1,250-1,300 ℃ assuming the water content of ~ 1.5 wt.% (Figure 8g). When the pressure and temperature respectively decrease to 0.5 GPa and 1,200 ℃, the reacting melt has a higher viscosity of ~10.5 Pa·s. Additionally, there is no evident difference in melt viscosity between the melt source and the melt-peridotite interface. However, the addition of carbonate (PC560) potentially leads to a peculiarly lower melt viscosity (~ 0.25 Pa·s) estimated by using a simple model (Di Genova et al., 2014) under the assumption of the 2 wt.% carbonate dissolved in silicate melt, which represents an order-of-magnitude evaluation of the melt viscosity due to the uncertainty of extrapolation (Figure 8g).

Except for several large sulfide droplets containing the Ni-rich quenched phases, the composition of sulfide was homogeneous in the lower melt source of all experiments. In the 12 h experiment, the S content, Ni/S and Fe/S ratios of sulfide liquid were ~ 35.16 ± 0.72 wt.%, ~ 0.39 ± 0.03, and ~ 1.43 ± 0.04, respectively, and these values remained constant within the error of measurement when the annealing time increases to 72 h (S ~ 35.74 ± 0.74 wt.%, Ni/S ~ 0.37 ± 0.09, Fe/S ~ 1.42 ± 0.06). However, the Cu/S ratio of sulfide liquid slightly decreased from 0.017 ± 0.004 at the 12 h to 0.009 ± 0.002 at the 72 h at 1,250 ℃, while an obvious increase in the Cu/S ratio (~ 0.046 ± 0.010) was observed at 1,300 ℃ (Table S4).

4 Discussion

4.1 Grain-scale processes in melt-peridotite reaction

Firstly, if the upper peridotite reaches equilibrium at 1.5 GPa and 1,250-1,300 ℃, the corresponding melt fraction will be less than 0.04-0.08 wt.% based on the thermodynamic model via the pMELTS (Ghiorso et al., 2002), implying that the self-partial melting of peridotite at the experimental conditions is negligible here. The observed variations of melt area fraction, phase proportions, and minerals' sizes and compositions in our experiments can be primarily attributed to the melt-peridotite reaction. On the other hand, the upper peridotites are not in equilibrium with the starting melts at the experimental conditions, and hence olivine and clinopyroxene in the peridotite part should partially or completely dissolve in the reacting and upward percolating melt (Liang, 1999; C. Wang et al., 2020). In multicomponent partially molten systems, the melt-peridotite reaction is suggested to occur via multi-scale mass transfer processes that inevitably

involve both the grain-scale dissolution-precipitation-reprecipitation and diffusion, in conjunction with large-scale advective transport (Cascio et al., 2008; Morgan & Liang, 2005).

In our high-temperature, high-pressure experiments (1.5 GPa and 1,250-1,300 °C) here, due to the disequilibrium between melt and peridotite, the consequent grain-scale processes can mostly occur via the dissolution, precipitation, and reprecipitation of mineral grains, which is evident from the formation of ORL. In the lower melt source, the basaltic melt in starting materials is olivine-undersaturated, and thus the melt-rock reaction between basaltic melt and olivine produces new Opx grains (Figure 1), which is consistent with the following reaction:

$$melt_0 + Ol_0 \longrightarrow melt_1 + Opx_1 \quad (1)$$

where subscripts 0 and 1 designate melt and mineral grains from starting materials and the reaction products, respectively. This reaction should occur via the dissolution of olivine, and precipitation of new orthopyroxene, largely contributing to the formation of ORL in the interface between the peridotite and melt source (Figure 1a). It is well known that dissolution and precipitation occur simultaneously during the development of the ORL under high pressure (> 1 GPa) (Cascio et al., 2008; Morgan & Liang, 2003). With increasing the degree of melt-peridotite reaction (a longer run duration and/or higher temperature), an olivine-melt layer above the ORL is formed by the further dissolution of olivine and few clinopyroxene grains, with concomitant reprecipitation of fresh olivine grains in the melt reaction flow (Figure 2) (Kelemen et al., 1995).

The grain size of silicate minerals plays a vital role in affecting the physical properties of upper partially molten peridotite, such as permeability (Faul, 2001). Here, the growth of silicate mineral sizes in the upper partially molten peridotite with increasing annealing time (Figure 4b) is mostly driven by a reduction of grain boundary energy (Faul & Scott, 2006) and demonstrates that textural coarsening by which small-size crystals are consumed to support the growth of coarser grains (Higgins, 1998, 2011; Yao et al., 2017), may overweigh the decreasing-size effect related to reprecipitation of new, fine-grained crystals. The transference of material from dissolved olivine to other grains occurs via diffusion through grain boundaries, crystals themselves, and interstitial melt (Yao et al., 2017), while the last one is much faster and becomes the main pathway of these grain-scales processes. Finally, large-scale advective transport of

reacting melt is evident from the variations of melt area fraction in the partially molten peridotite and the formations of melt junctions and channels (Figure 1; Figure 4a).

Based on the parabolic law of diffusive dissolution (Liang, 1999; Zhang et al., 1989), the slope (*i.e.*, the diffusive dissolution constant) of the fitted linear regression line for our experiments is used to estimate the growth rate of ORL (k_{ORL}), which is about ~ 0.78 ± 0.05 μm/s$^{0.5}$ at 1.5 GPa and 1,250 °C. This growth rate is far lower than those of some previous experiments conducted at higher temperatures and/or pressures (Figure 3a) (Morgan & Liang, 2005; C. Wang et al., 2020). The thickness of ORL in experiment PC527 at 1.5 GPa and a higher temperature (~ 1,300 °C) has a faster-increasing tendency (k_{ORL} = 2.37 ± 0.14 μm/s$^{0.5}$), consistent with the experiments under 2 GPa and 1,375 °C (C. Wang et al., 2020). This tendency of ORL growth is likely unchanged in the experiments with the carbonate-bearing melt source (PC560) and silicate melt-bearing peridotite (PC548) (Figure 3a), implying an insignificant effect of melt composition and porosity on the growth of ORL. Our results indicate that the increase in temperature will potentially enhance the growth rate of ORL thickness during the melt-rock reaction, which can be mostly attributed to the higher diffusivities of elements in silicate melts at a higher temperature (Mungall, 2002; Zhang et al., 2010).

Similarly, we observed the linear increase of dissolution distance with the square root of time (Figure 3b), suggesting that a substantial amount of peridotite was dissolved in the percolating melt. At 1.5 GPa and 1,250 °C, the dissolution rate of peridotite evaluated by the slope of the linear regression line (k_{diss} = 0.58 ± 0.08 μm/s$^{0.5}$) is lower than those in previous experiments with higher temperatures and pressures (Figure 3b, C. Wang et al., 2013, 2020), indicating that relatively high temperature also increases the dissolution rate. Moreover, the higher dissolution rate of peridotite at experiment PC527 (1,300 °C) implies that an increase in temperature significantly enhances melt-rock reaction (Mitchell & Grove, 2016). The high content of water (~ 1.57 ± 0.15 wt.%) in silicate melt could enhance the formation of several enormous Opx grains in the ORL (Figure 2) (Wang et al., 2016), partly because the addition of water can strongly depress the peridotite solidus. This may be also the reason for the large standard deviations of the dissolution rate in experiments PC527 and PC545 with a high temperature (1,300 °C) and long annealing time (72 h). Overall, the growth rate of the ORL is generally higher than the peridotite dissolution rate, which is potentially attributed to the volume-increasing reaction during the replacement of olivine by orthopyroxene (Milke et al., 2009).

4.2 Compositional variations of melt and minerals

During a melt-peridotite reaction, besides the systematic changes in mineralogy and texture of peridotite, we also observed the compositional variations of melt and minerals in the reaction couple (Figures 6-8), which have been widely used to outline the grain-scale processes governing this melt-peridotite reaction (Mallik & Dasgupta, 2012; C. Wang et al., 2020). On the other hand, a thermodynamically-constrained mixing model has been recently used to examine the variations of major element compositions of minerals during the melt-peridotite interaction (Lambart et al., 2012; Pin et al., 2022; Shaw et al., 2018), and this forward model may offer a key to testing and understanding the compositional evolution of our experimental products.

The melt-peridotite reaction here is modeled as a simplified, thermodynamic process in which the peridotite is continually impregnated by a finite amount of basaltic melt from the lower melt source, which is the same as the assumption in previous works (Lambart et al., 2012; Pin et al., 2022; Shaw et al., 2018). After each increment of melt impregnation, the infiltrated melt will eventually be equilibrated with surrounding peridotite, and the thermodynamic properties of the whole system are adopted as a reference for the next increment. In each increment, the proportions and compositions of melt and solid phases after chemical re-equilibrium can be obtained by finding the minimum Gibbs energy of the whole system (Pin et al., 2022; Yao et al., 2018). This process is modeled by constantly adding up to 200 g of the lower basaltic melt by increments of 0.5 g, to 100 g of the upper peridotite, using the pMELTS of alphaMELTS (Ghiorso et al., 2002; Ghiorso & Sack, 1995; Smith & Asimow, 2005) in isenthalpic mode at 1.5 GPa, 1,250-1,300 °C and ΔQFM-2.0. Here, the incremental addition of basaltic melt corresponds to the increase of melt: peridotite ratio from 0.005 to 2.

Our simulation shows that the mass fraction of olivine decreases from ~ 49 wt.% to ~ 22 wt.% with the increasing melt: peridotite ratio from 0.005 to 2 (Figure 8h). The silicate melt becomes saturated with orthopyroxene when the melt: peridotite ratio reaches ~ 0.22. After this point, the mass fraction of new orthopyroxene precipitated from silicate melt quickly increases to ~ 32 wt.% at the melt: peridotite ratio of 2 (Figure 8h). The mass fraction of clinopyroxene in peridotite has a quick increase from ~ 51 wt.% to ~ 57 wt.% before the precipitation of orthopyroxene, but then slowly decreases to ~ 46 wt.% at melt: peridotite ratio = 2 (Figure 8h). Hence, the increase in orthopyroxene proportion is mostly due to the dissolution of olivine,

accompanied by a limited contribution from the consumption of less than ~ 5 wt.% clinopyroxene, which approximatively coincides with the hypothetical Reaction 1 mentioned above.

Concurrently, the melt penetrates upwards and further reacts with the peridotite to result in systematic variations of the compositions of olivine and Cpx grains towards the melt-rock interface (Figure 6 and Figure 7). The modeled compositional evolutions of olivine show a decreasing trend of MgO content from ~ 49.3 wt.% to ~ 44.1 wt.%, an increase of FeO content from ~ 9.0 to ~ 14.5 wt.%, and the associated decrease of Mg# from ~ 90.7 to ~ 84.4, when the melt: peridotite ratio increases from ~ 0.005 to ~ 1.5 (Figure 6h). In the same range of melt: peridotite ratio, the clinopyroxene has an obvious increase in its MgO content (from ~ 17.5 to ~ 20.0 wt.%) and approximately constant Al_2O_3 content (Figure 7h). The trends of these compositional variations of minerals are nearly in agreement with those of our experiments, except for the low-pressure experiment (PC559, Figure 6h and Figure 7h). Therefore, the measured compositional variations of olivine and clinopyroxene as a function of distance away from the final melt-peridotite interface may be connected to the melt: peridotite ratio during the reaction. The measured compositions of olivine and Cpx grains just above the final melt-peridotite interface are approximately consistent with those results simulated thermodynamically (Figures 6h and 7h-gray shadow regions) in the melt-peridotite ratio of 1.0 to 1.5, which implies that they have obtained locally chemical re-equilibrium with the reacting melt that is about ~ 1.0-1.5 times the initial mass of peridotite in the same region. As the distance away from the final melt-peridotite interface grows, the growing MgO and Mg# contents of olivine reflect the decrease of melt: peridotite ratio, and consequently imply the gradual weakening of melt-peridotite reaction. Therefore, when the upward-flowing melt encounters the partially molten peridotite that initially has a low permeability, melt convection, backflow, and the associated high-degree melt-peridotite reaction mostly occur at the bottom of peridotite, leading to an increase of porosity of the reaction region and more motivation of upward melt flow. This potentially produces positive feedback between the reaction and melt flow, contributing to upward infiltration of more silicate melt into the partially molten peridotite.

Along with the increasing melt: peridotite ratio from ~ 1.0 to ~ 1.5, the modeled silicate melt that is reacted with the peridotite shows a decrease of SiO_2 content from ~ 47.1 wt.% to ~ 46.7 wt.%, which is partly less than the measured ranges in our experiments with long annealing

time (Figure 8a). The Al_2O_3 content of silicate melt varies from ~ 13.6 wt.% to ~ 13.1 wt.%, while the MgO content of melt shows a narrow variation range of ~11.1 wt.% to ~11.4 wt.%, which both roughly match our experiments (Figures 8b and 8e). The possible iron loss to Pt capsule in these experiments due to the incomplete isolation of separate upper and lower graphite capsules with different diameters for silicate melt from Pt capsule (J. Wang et al., 2020) is likely to be the main reason for the lower FeO content (Figure 8c) measured in these experiments with long annealing time (> 48 h). The model suggests that silicate melt contains ~ 7.6-7.9 wt.% CaO at the melt-peridotite of 1.0-1.5, but this range is underestimated in contrast to our measurements (Figure 8d), partly because of the slight differences in the Gibbs free energy among various compositional models of pyroxenes (Yao et al., 2021) may drive large errors in the CaO content of clinopyroxene in the AlphaMELTS. Although there still have some weaknesses in modeling the compositional evolution of melt, the use of AlphaMELTS is encouraging here and helps to examine how mineral modes and chemical compositions evolve as silicate melts are added into the upper peridotite part.

4.3 Coarsening processes of sulfide droplets

In a partially molten system, the nucleation/growth rate and associated size distribution of sulfide droplets are vital constraints on their dynamics (Yoshino & Watson, 2005). Along with the increasing annealing time, the size of sulfide droplets shows a larger increase (from ~3.2 ± 0.1 μm to ~11.1 ± 0.4 μm) (Figure 5c) compared with that of the surrounding silicate minerals (from ~8.1 ± 3.4 μm to ~11.0 ± 4.9 μm) (Figure 4b). The growth of silicate minerals has been suggested to be mostly controlled by the melt-enhanced diffusion of material, but sulfur that is the one of major elements in the sulfide has a much lower diffusivity than those of other elements (Freda et al., 2005; Yao & Mungall, 2021). Given that the diffusion of S rather than Fe limits the growth rate of sulfide droplets (Zhang, 2015), slow growth is expected for sulfide if its growth completely occurred via element diffusion. However, the estimated growth rate of sulfide droplets is larger than those of silicate minerals in our measurements, suggesting that there must be other mechanisms, besides the diffusion-driven growth, contributing to the fast growth of sulfide droplets.

On the other hand, the actual 3D size distribution of sulfide droplets in the melt source shows a uniform, nearly log-normal size distribution with a skewed peak to a slightly smaller

size than the average one (Figure 9), which can be attributed to the possible contribution of the Lifshitz-Slyozov-Wagner (LSW) coarsening and the occurrence of normal grain growth (Honour et al., 2019; Yoshino & Watson, 2005). Based on the classical LSW theory (Lifshitz & Slyozov, 1961; Wagner, 1961), the kinetics of crystal growth can be approximately described as $r \sim t^{1/m}$, where r is the grain size, with the exponent $m = 3$ for a diffusion-controlled process and $m = 2$ under the control of an interface reaction. At 1,250 ℃ and 1.5 GPa, growth rates of sulfide droplets are slightly slower than that predicted ($m = 2$) by the interface-reaction-controlled process via a transient regime ripening before static-state ripening (Figure 5a), implying the likely combination of multiple coarsening processes here (Lautze et al., 2011; Sun, 2007). High run temperature (1,300 ℃) can contribute to a higher degree of interface-controlled reaction (Yoshino & Watson, 2005), which potentially facilitates the coarsening processes of sulfide in the melt source (Figure 5a). A dramatical decrease in the number density of sulfides (Figure 5a-inset) and the presence of sulfide droplets in contact with each other (Figure 2b and Figure S1), both imply that the contribution of mechanical coalescence of sulfides (agglomeration and successive coalescence) to their coarsening processes may be more important at droplet contacts (Yoshino & Watson, 2005). Moreover, the coalescence of sulfide droplets is enhanced at lower viscous melts (Holzheid, 2010), potentially addressing a significant increase in growth rate (Figure 5a) from the carbonate-bearing experiment (PC560) with a lower melt viscosity (Figure 8g) (Di Genova et al., 2014). Although the previous analog experiment (de Bremond d'Ars et al., 2001) and static high-temperature, high-pressure experiments (Bockrath et al., 2004; Holzheid, 2010) did not observe the aggregation of sulfide droplets, their mechanical coalescence, for the first time, has been demonstrated to be feasible in our experiments with strong melt convection and melt-peridotite reaction. This mechanical coalescence may occur via the impaction of sulfide droplets with each other, and further drainage and rupture of the infinitesimally liquid film separating them in the reacting melt flow, as suggested by theoretical analyses (Yao et al., 2019).

5 Implications

5.1 Porous melt flow in the partially molten peridotite

These dissolution-reprecipitation processes not only change the composition and proportion of solid phases, but also increase the porosity of peridotite in the upper part of samples, thereby enhancing upward mobilities of silicate melt and sulfide droplets away from the

lower melt source (Figure 4 and Figure 5). Moreover, the porosity of ORL is enough high for the entrainment of sulfide droplets into peridotite (Figure 1 and Figure 2). In addition, with increasing annealing time to 72 h, more basaltic melt infiltrating into the peridotite region from the melt source (Figure 4) could potentially enhance the reaction between basaltic melt and peridotite. This melt-rock reaction may produce a high flow capacity of reacting melt through a dissolvable peridotite (Chadam et al., 1986; Jackson et al., 2018), resulting in the formation of the finger- or tree-like melt-rich channels in which a fast-ascending magma flow can even drive the antigravitational migration of coarse olivine grains (Pec et al., 2017). Hence, the development of positive feedback between the enhanced permeability and the associated increase of melt flux in reacting regions produces a higher flow velocity of melt and the wider melt channels among crystal framework (Aharonov, 1995; Pec et al., 2017), thereby potentially facilitating the upward entrainment of sulfide droplets (Wang & Jin, 2020).

To quantitatively outline the upward physical migration of sulfide droplets along with the reactive melt flows in the dissolvable peridotite, some theoretical parameters of physical properties of the partially molten peridotite should be considered first (*e.g.*, von Bargen & Waff, 1986; Mckenzie, 1984). For an ideal porous crystal framework, the permeability (k) can be cast by using a power-law relationship between grain size (d) and porosity (Φ) of the crystal matrix (von Bargen & Waff, 1986):

$$k=\frac{\Phi^n d^2}{C} \tag{2}$$

where C and n are constant parameters depending on the topology of the melt phase and the geometry of an individual melt channel. Based on the previous works (Miller et al., 2014; Z. Wang et al., 2020), some suitable ranges of C (36-94) and n (2.4-2.8) are used for our experiments that contain the multiphase-mineral assemblage.

On the basis of the numerical model from McKenzie (1989), the extraction velocity of melt relative to the stationary crystal framework can be estimated by:

$$v=\frac{k\Delta\rho_m g}{\Phi\mu_m} \tag{3}$$

where $\Delta\rho_m$ - the density contrast between silicate melt and solid mineral, g - the gravitational acceleration, and μ_m - the melt viscosity, which decreases with increasing temperature and volatile content (mainly CO_2 and H_2O) (Dingwell, 1996; Di Genova et al., 2014). Based on equation (2) and (3), the porous flow velocity of melt through grain-scale percolation is ~ 0.74 μm/h in the partially molten peridotite of experiment PC545 (C ~ 36, n ~ 2.6, Miller et al., 2014; Φ ~ 7.13 %; μ_m ~ 2.2 Pa·s; d ~ 11.0 μm; $\Delta\rho_m$ ~ 600 kg/m^3, g ~ 9.8 m/s^2). Apparently, the transport distance (~ 53.3 μm) of this slow-extracting (~ 0.74 μm/h) melt within the longest experimental time (72 h) is much shorter than the region of melt-peridotite reaction observed here (Figure 1a), which implies that other mechanisms of melt extraction occur concurrently to drive a higher flow velocity. In addition to the melt junctions among minerals, we also observed thick melt channels (Figure 2) between some opening mineral grain boundaries in the ORL and olivine + melt layer where a new crystal framework may have not been built, indicating the possible existence of melt channelized flow, which has been demonstrated by some experimental studies (*e.g.*, Pec et al., 2017; Zhu et al., 2011) and the field investigations on dunite channels in MORB (*e.g.*, Kelemen et al., 1995). Melt velocity in these channels is suggested to be much higher relative to other regions (Pec et al., 2017; Wang & Jin, 2020).

We then extrapolate our experimental results to the partially molten mantle. Generally, the porosity (Φ) is approximately estimated to be ~ 1 – 15 % in the partially molten peridotite (*e.g.*, Mei et al., 2002; Yoshino et al., 2010; Zhu et al., 2011), and the regions having high-degree melt-rock reaction can obtain a higher porosity (Pec et al., 2017). Hence, the Φ in our model of the molten mantle is properly set as 3 – 20 %. The observed grain size of upper mantle peridotite is about mm-scale (Ave Lallemant et al., 1980; Karato, 1984), and thus the crystal radius in our model is set as ~ 1.5 mm, which is about two orders of magnitude higher than the grain size (~ 10 μm) in the experiments here. Therefore, the permeability of upper mantle peridotite should be much better than the estimated situation of our experiments, and consequently, the extraction velocity of melt relative to stationary crystal framework in the residual mantle increases to ~ 4.78×10^{-6} – 5.62×10^{-5} m/s (~ 150.81 – 1,771.06 m/year) with the growth of Φ from 3 to 20 %, if other parameters in equation (3) remain constant. On the other hand, the melt transport velocities within the mantle were estimated to have a wide range of 1 to 1,000 m/year by analyses of uranium-series (U-series) disequilibria in lavas and Icelandic deglaciation (Katz et al., 2022; Rees Jones & Rudge, 2020; Rubin et al., 2005). The channelized melt flow potentially

has a higher melt extraction velocity, which can even reach ~ 10,000 m/year (McKenzie, 2000). In contrast, recent laboratory experiments further estimate some conservative velocities of the porous melt flow (~ 2.4 – 29.7 m/year, Z. Wang et al., 2020; ~ 2 – 150 m/year, Connolly et al., 2009; ~ 0.5 m/year, Zhu et al., 2011). The estimated melt velocity (~ 150.81 – 1,771.06 m/year) here is higher than the previous experimental results (~ 0.5 – 150 m/year), but falls into the potential range of melt flowing velocity (~1 – 10,000 m/year) in the natural mantle. The wide range of melt flowing velocity can be attributed to the heterogeneous grain size, various mineral phases, and associated heterogeneous melt flow in natural peridotite relative to these in experimental conditions.

The microstructure of a porous crystal framework is usually simplified as a "throat and chamber" model, where the interstitial chamber pores are connected by many narrow throat pores. The size distribution of these throat pores will have a great effect on the permeability of the crystal framework, which in turn determines the percolation of silicate melt and the migration of sulfide. Previous numerical models had demonstrated that the ratio of mean throat pore radius to mineral radius decreases from 0.24 to 0.09 along with the decreasing porosity of crystal framework from 35.4% to 8.3% (Sweeney & Martin, 2003). Based on this modeling result, we can estimate the variations in the mean throat pore radius of the partially molten peridotite with constant crystal size (~ 1.5 mm) and variable porosity due to the melt-rock reaction, which can help us to trace the dynamic migration of sulfide in crystal framework.

5.2 Upward entrainment of fine sulfide droplets by porous melt flow

The physical mobility of sulfide liquids along with a sulfur-saturated silicate melt within the crystal framework of partially molten peridotite largely depends on the size of sulfide droplets, the permeability of crystal framework, the connectivity of melt network, and the processing degree of melt-rock reaction (Z. Wang et al., 2020; Yao & Mungall, 2020). Chung & Mungall (2009) simplified the downward sinking of sulfide droplets in the crystal framework, and proposed that this process is mostly controlled by the relative sizes of sulfide droplets and surrounding crystals within partially molten peridotite. In this regard, for the upward transport of a sulfide droplet, its terminal settling velocity should be also less than the upward velocity of porous melt flow, although its size has been smaller than the size of the most constricted part of the melt channel or pore throat in the crystal framework. The terminal settling velocity of the

spherical droplet will achieve when its gravity-driven buoyance force (F_B) is balanced by the vertical drag force (F_D).

The melt flows passing through sulfide droplets that are nearly stranded in the melt channel or port throat, as a first approximation, is regarded as the flow of an incompressible fluid around a circular cylindrical particle (*i.e.*, the sulfide droplet) confined by two parallel flat plates (*i.e.*, the melt channel) (Figure 10a) (Lee & Fung, 1969). The drag force (F_D) acting on this sulfide droplet can be expressed by a dimensionless coefficient (f_D):

$$F_D = f_D \times 4\pi\mu_m UR \quad (4)$$

where R is half the distance between the two plates, *i.e.*, the radius of the melt channel, and U is the stokes flow velocity of melt around sulfide droplet. Based on the modeling results from Lee & Fung (1969), the dimensionless coefficient, f_D, can be estimated via the ratio between R and r_s which is the radius of an initial undeformed sulfide droplet before entering the melt channel (Figure 10b). For simplification, here we assume that the spherical droplet has a radius (r_s) equaling to or being slightly higher than R, and thus the corresponding values of f_D should exceed ~ 4.8 (Figure 10b) (Lee & Fung, 1969).

On the other hand, dense sulfide droplet always has a trend of settling to the base of the capsule due to gravity, and the corresponding buoyancy force (F_B) can be expressed as:

$$F_B = \frac{4}{3}\pi r_s^3 g \Delta\rho_s \quad , \quad (5)$$

where $\Delta\rho_s$ = 1,700 kg/m^3 is the density difference between sulfide and silicate melt (Kress et al., 2008; Z. Wang et al., 2020). Hence, the velocity of melt flow that just successfully entrains sulfide droplets whose sizes are close to that of melt channel/pore throat can be calculated via:

$$U = \frac{F_D}{4\pi\mu_m R \cdot f_D} = \frac{F_B}{4\pi\mu_m R \cdot f_D} = \frac{r_s^3 g \Delta\rho_s}{3\mu_m R \cdot f_D} \quad , \quad (6)$$

Because the measured maximum radius of sulfide droplets in the upper peridotite part is ~ 9.5 μm, the maximum value of U is estimated as ~ 170.9 μm/h (~ 1.5 m/year), when the R/r_s equals 1. This value can represent the localized velocity of channelized melt flow in the regions

of melt-rock reaction and is nearly three orders of magnitude higher than the velocity of melt porous flow (~ 0.74 μm/h) driven by compaction of crystal framework. As the melt flow velocity is changeable due to the complex morphology of interconnected melt channels and variable fluid dynamic environments in porous peridotite (McKenzie, 1989; Miller et al., 2014; Z. Wang et al., 2020; Zhu et al., 2011), our calculation (~ 1.5 m/year) here is used as an order of magnitude estimate for the velocity of melt flow around sulfide droplet through narrow pore throat in these experiments.

When the porous melt flow in crystal mush has a small velocity, it may not have enough kinetic energy to overcome the gravitational settling of large sulfide droplets. Hence, in this case (the region of No. ① in Figure 11), the maximum size of the upward migrating sulfide droplet is mostly controlled by the low flow velocity when the droplet size is smaller than the pore throat at the high porosity of crystal mush. For the porous melt flow with a velocity of ~ 5.1×10^{-6} m/s (~ 161 m/year), due to the balance between F_B and F_D, the corresponding sulfide droplet radius is about 98.2 μm, which is less than the mean radius of pore throat in crystal mush with increasing Φ from 3 to 20% (Figure 11). Here, the maximum radius (r_s) of sulfide droplets that can pass through the crystal mush will remain at ~ 98.2 μm even though the permeability of crystal mush has been highly improved due to the increasing porosity. When the velocity of porous melt flow increases to ~ 11.6×10^{-6} m/s (~ 366 m/year), the r_s is limited by the radius of the narrow pore throat at low porosity (about ~ 9%), but keeps a constant value (~ 148.5 μm) at a higher porosity (Figure 11). A further increase in the porous melt flow velocity (*e.g.,* ~ 2.1×10^{-5} m/s, ~ 662 m/year) will further reduce the porosity range (> ~ 15%) of which the r_s is just related to the melt flow velocity (Figure 11).

Once the melt velocity increases to ~ 3.2×10^{-5} m/s (~ 1,009 m/year), the value of r_s due to the balance between F_B and F_D will increase to ~ 246.7 μm, which is equal to the radius of pore throat at Φ = 20% (Figure 11). Hence, if the melt velocity is beyond this value, the motivation of porous melt flow is no longer the restriction on the upward transport of fine sulfide droplets whose sizes are less than the radius of pore throat in crystal mush with the porosity range of 3-20%. Of course, this moderate flow velocity cannot provide enough power to overcome the capillary forces preventing droplet deformation as the coarse sulfide droplets attempt to pass into pore throats narrower than themselves. Therefore, in this situation (the No. ② in Figure 11), the sizes of upward transporting sulfide droplets must be strictly no larger than

676 the pore throat size in the crystal mush. Because the mean size of the pore throat is just related to
677 the grain size and porosity of molten peridotite based on the modeling results from Sweeney &
678 Martin (2003), the value of r_s should be equal to the estimated pore throat size that increases
679 from 99.7 to 246.7 μm with the increasing porosity from 3 to 20%, which is irrelevant to the melt
680 flow velocity. Thus, the No. ② situation is represented by a black line in Figure 11, although the
681 corresponding flow velocity may vary from ~ 3.2×10^{-5} m/s (~ 1,009 m/year) to a much higher
682 value (*e.g.,* ~ 0.08 m/s, as explained below). Hence, during the melt-peridotite reaction, the
683 accompanying melt flow in the dissolved peridotite is energetic, and its flow velocity seems to be
684 high enough to drive the upward transport of fine μm-scale sulfide droplets (Figure 10c-right
685 side; Figure 11).

686 5.3 Potentially upward transport of coarse sulfide droplet

687 When a coarse sulfide that is sufficiently larger than the minimum constriction of the
688 melt channel is gradually squeezed into the small "throat" part along with the ascending reactive
689 melt flow, the sulfide droplet will invade this throat and be changed to a pear shape having a
690 smaller radius of curvature (Figure 10c-left side). Obviously, the upward migration of this coarse
691 sulfide droplet in the partially molten peridotite becomes complicated, and the referred dynamic
692 process simplistically involves a competition between buoyancy, pressure gradient, viscous,
693 capillary, and drag forces (Yao & Mungall, 2020). This squeezing process introduces the
694 additional capillary pressure P_c, which is a measure of the pressure discontinuity existing at the
695 interface of two immiscible phases (Chung & Mungall, 2009). The additional pressure imposed
696 on this deformed sulfide droplet within the squeezing process equals the difference in capillary
697 pressure between the top and bottom interfaces of the sulfide droplet and can be calculated by:

698 $$\Delta P_c = 2\gamma_{ms} \times \left(\frac{1}{r_t} - \frac{1}{r_d}\right) \quad (7)$$

699

700 where γ_{ms} = 0.21 N/m is the melt-sulfide surface tension (Mungall et al., 2015), r_t is the radius of
701 the upper spheric cap, and r_d is the radius of the lower part of the pear-shaped droplet (Figure
702 10c). The droplet cannot be forced through the pore throat unless this excess pressure ΔP_c is
703 balanced by an equal or greater pressure (ΔP) exerted by ascending melt flow on the trailing
704 edge of sulfide droplet, which tends to push the droplet to rise through the melt channel.

Because the silicate melt flows at a low Mach number, the simple form of Bernoulli's principle is valid for the quasi-incompressible flows in melt-peridotite reaction, and hence pressure of flowing melt around a sulfide droplet can be highly related to the peripheral flow velocity via the Bernoulli's equation (Bauman & Schwaneberg, 1994):

$$P_1 + \frac{\rho_m U_1^2}{2} + \rho_m g h_1 = P_2 + \frac{\rho_m U_2^2}{2} + \rho_m g h_2 \quad (8)$$

where the subscripts 1 and 2 correspond to the top and bottom outside points of deformed sulfide droplets along the axis of symmetry, respectively; P is the pressure caused by the flow of silicate melt; ρ_m is the density of melt; h is the height of 1 and 2 relative to a reference point beneath sulfide droplet. Hence, the flowing-melt-driven external pressure imposed on the deformed sulfide droplet equals the difference (ΔP) between P_1 and P_2. In an extreme case, the coarse, deformed sulfide droplet completely blocks the ascending melt flow, and the flow velocity at bottom of droplets (U_2) is close enough to zero, leading to a maximum value of external pressure difference (ΔP) that can be calculated as:

$$\Delta P = P_2 - P_1 = \frac{\rho_m U_1^2}{2} + \rho_m g(h_1 - h_2) = \frac{\rho_m U_1^2}{2} + \rho_m g \Delta h \quad (9)$$

where U_1 is the flow velocity of melt at the top of the sulfide droplet, and Δh is the vertical distance between the top and bottom points of the droplet. Assuming that the volume of a sulfide droplet is unchanged during the squeezing process, the height of this invading sulfide droplet (Δh) can be described by Chung & Mungall (2009):

$$\Delta h = r_t + r_d + \sqrt{r_d^2 - R^2} - \sqrt{r_t^2 - R^2} \quad (10)$$

For the deformed sulfide droplet, it bears the upward pressure driven by flow melt (*i.e.*, ΔP), which should balance or even exceed the total of downward capillary pressure (ΔP_c) and gravity-driven pressure (P_G) for the droplet to rise through the constriction:

$$\Delta P \geq P_G + \Delta P_C = \rho_S g \Delta h + 2\gamma_{ms} \times \left(\frac{1}{r_t} - \frac{1}{r_d}\right) \quad (11)$$

where ρ_s is the density of sulfide liquid. Thus, combining the above equations (7-10), under the critical condition for migration of sulfide droplet into the pore throat to be the case (r_t = R) (Chung & Mungall, 2009), the equation 11 substituted with the appropriate values for ρ_m = 2,600 kg/m^3 (Robertson et al., 2016) is simplified into:

$$1{,}300 \times U_1^2 \geq 16{,}660 \times \left(R + r_d + \sqrt{r_d^2 - R^2}\right) + 0.42 \times \left(\frac{1}{R} - \frac{1}{r_d}\right) \quad (12)$$

And finally, the initial radius (r_s) of this sulfide droplet before its invasion into the pore throat can be calculated by Chung & Mungall (2009):

$$r_s = \left(0.5 \times \left(r_d^3 + R^3 + \left(r_d^2 + \frac{1}{2}R^2\right) \times \sqrt{r_d^2 - R^2}\right)\right)^{1/3} \quad (13)$$

When the melt flows around a sulfide droplet through a narrow pore throat in the partially molten peridotite, the associated velocity field is suggested to be not homogeneous. In addition, it is well known that exactly deciphering the flow velocity field of silicate melt infiltrating through a multi-mineral phase system plays a critically important role in understanding the geodynamic properties of the partially molten upper mantle, but it is challenging and beyond the scope of this study. The increases in grain size and permeability may also strongly enhance the melt flow velocity in the new channel of the crystal framework. Here, the flow velocity in the channel has been confirmed to be about three orders of magnitude higher than that of porous flow through grain-scale percolation in our experiments, which may be extrapolated to the mm-scale upper mantle peridotite. Therefore, the velocity of melt flow around a sulfide droplet in the channel in upper mantle peridotite may be in the magnitude of 0.001-0.1 m/s, and thus the local velocity (U_1) of focused melt flow around the top of a sulfide droplet was analogously assumed as ~ 0.3 m/s and ~ 0.08 m/s here (Figure 11- region ③) for the localized high-degree melt-rock reaction regions of the partially molten mantle. This range of flow velocity is also consistent with the estimates from previous studies discussed in Section 5.1.

Equations 12 and 13 are numerically solved for the above value of U_1 by programming a loop using Maple©. Based on the above numerical calculation, when the velocity of focused melt flow around a sulfide droplet is less than ~ 0.08 m/s, the sulfide droplet is difficult to overcome the capillary pressure imposed by melt channel/pore throat with a smaller size, and will be

761 stranded in inter-grain pores. However, these flow velocities (~ 3.2×10^{-5} m/s – 0.08 m/s) are
762 still large enough to drive upward transport of sulfide droplets whose radii are smaller than or
763 almost the same as the radius (R) of pore throat (Figure 11-region ②).

764 For a powerful melt flow with extremely high velocity (*e.g.*, ~ 0.3 m/s in Figure 11-
765 region ③), coarse-grained sulfide droplet overcomes the capillary pressure driven by the pore
766 throat, and its maximum radius for upward migration increases from ~ 106.8 to ~ 276.8 μm with
767 increasing the porosity from 3 % to 20 % (Figure 11-region ③), which is larger than the
768 corresponding radius of the pore throat (from ~ 99.7 to 246.7 μm). In this condition (region ③ in
769 Figure 11), the coarse sulfide droplets can pass through the pore throat narrower than themselves.
770 Although the estimates of the maximum sulfide size that are capable of upward migrating
771 through the porous molten peridotite are divided into three conditions along with the increasing
772 melt flow velocity (the regions ①-③ in Figure 11), all of them are mostly dominated by the melt
773 flow velocity, porosity, and grain size of peridotite, which would be strongly enhanced by the
774 high-degree melt-rock reaction.

775 On the other hand, based on these previous studies on the abyssal and orogenic
776 peridotites, and peridotite xenoliths (*e.g.*, Lorand & Luguet, 2016; Lorand et al., 2010; Luguet et
777 al., 2003), highly variable grain size (< 20 μm to 500 μm) of sulfides is widely observed in the
778 upper mantle, while most sulfides are likely smaller than about 100 μm in diameter. Hence, it is
779 plausible that almost all sulfide droplets are stranded among the crystal framework of the upper
780 peridotite mantle with low porosity, while the high-degree partial melting and/or melt-peridotite
781 reaction will lead to high porosity, large flow velocity, and even the new-forming melt channel,
782 which highly proposes that efficient entrainment of most sulfide droplets into ascending magma
783 flow among porous peridotite is physically possible, especially among channelized extraction of
784 silicate melt in melt-peridotite reaction. Conceivably, mechanical entrainment of sulfide droplets
785 during the melt-rock reaction would be more efficient than the transport of sulfide liquid by
786 dissolving in departing silicate melt, especially given the slow S diffusion in the basaltic melt
787 (Freda et al., 2005). The sub-continental lithospheric mantle that undergoes large-scale partial
788 melting and melt-peridotite reaction under tectonically active craton margins may be favorable
789 conjunction of these factors and potentially conducive to the entrainment of large sulfide droplets,
790 thereby contributing to the fertilization of sub-continental lithospheric mantle and the primary
791 enrichment of metal-bearing sulfides for the formation of magmatic sulfide deposits (*e.g.*, Griffin

et al., 2013). This may be one of the reasons to account for the issue of why the spatial and temporal distribution of magmatic Ni-Cu-(PGE) sulfide deposits are genetically related to these regions (Maier & Groves, 2011).

6 Conclusions

Reaction-infiltration of silicate melt and concomitant transport of sulfide droplets in the partially molten peridotite are examined experimentally and thermodynamical-quantitatively in this study, which provides important insights into the fertilization of sub-continental lithospheric mantle and the efficient recycling of sulfur and metal elements from the partially molten mantle. The reaction between peridotite and basalt leads to the preferential dissolution of olivine and precipitation of orthopyroxene at high temperature (1,250-1,300 °C) and pressure (1.5 GPa), forming an orthopyroxene-rich reaction layer (ORL) with a high growth rate (~ 0.78 ± 0.05 $\mu m/s^{0.5}$ at 1,250 °C) in the melt-rock interface. With increasing the degree of melt-peridotite reaction, more silicate melt infiltrates through the ORL into the upper partially molten peridotite, forming an olivine-melt layer above the ORL, and coarse sulfide droplets could also be entrained along with the infiltration of silicate melt. Systematic variations observed in the compositions of minerals and reactive melt are approximately consistent with the thermodynamically-constrained mixing model. Meanwhile, the sizes of sulfide droplets have fast growth in the melt source, which is partly attributed to the multiple coarsening processes (including the mechanical coalescence) of sulfide droplets in the dynamic reactive melt flow.

Suspension and entrainment of sulfide droplets in the partially molten peridotite indicate a fast-flowing velocity of reactive melt (~ 170.9 μm/h) in our experiments, which demonstrates the occurrence of focused melt flows with high velocity in the reactive-forming melt channels, besides the melt porous flow driven by the density difference between silicate melt and minerals forming the crystal framework. It is convincible that the melt flow velocity within the melt-rock reaction is potentially high enough to drive upward transport of fine sulfide droplets with smaller diameters than that of the pore throat in the partially molten peridotite. In this condition, the maximum size of sulfide for upward entrainment is limited by the radius of the pore throat in the crystal framework of peridotite and increases with the growth of porosity during partial melting and melt-peridotite reaction. Only in the channelized melt flow with extremely high velocity, coarse-grained sulfide droplets could upward migrate through the pore throats narrower than

822 themselves. Hence, the high-degree melt-rock reaction regions in the upper mantle, such as the
823 sub-continental lithospheric mantle of craton margins, are likely to have wide pore throats, high
824 porosity, and even channelized melt flow with high velocity, which can potentially drive upward
825 entrainment and/or extrusion of sulfide droplets in the partially molten mantle, and thereby
826 fertilize the lithospheric mantle and lead to the endowment of Cu- and Ni-bearing sulfide for the
827 formation of associated deposits.

828 **Acknowledgments**

829 We are grateful to two anonymous reviewers for their useful suggestions and comments. We
830 thank Prof. Zhang Jinsen and Dr. Wenlong Liu for their help with EPMA and EBSD analysis.
831 Especially, I appreciate my wife Shasha Guo for the support and help in my life, so that I could
832 do my research without any worries. This research was supported by the National Natural
833 Science Foundation of China (No. 42102057, 42272084, and 41902088), the Natural Science
834 Foundation of Hebei Province (No. D2021402019), the fund from SinoProbe Laboratory (No.
835 SinoProbe Lab 202219), and the Education Department Foundation of Hebei Province of China
836 (BJ2020023).

837 **Data Availability Statement**

838 Microprobe images used for the composition measurements and all data are shown in figures and
839 the supplemental materials are freely available online
840 (https://doi.org/10.6084/m9.figshare.22352632).

841 **References**

842 Aharonov, E. (1995). Channeling instability of upwelling melt in the mantle. *Journal of*
843 *Geophysical Research: Solid Earth*, *100*(B10), 20433–20450.
844 https://doi.org/10.1029/95JB01307
845 Alard, O., Lorand, J. P., Reisberg, L., Bodinier, J. L., Dautria, J. M., & O'Reilly, S. Y. (2011).
846 Volatile-rich metasomatism in Montferrier xenoliths (Southern France): Implications for the
847 abundances of chalcophile and highly siderophile elements in the subcontinental mantle.
848 *Journal of Petrology*, *52*(10), 2009–2045. https://doi.org/10.1093/petrology/egr038

Ave Lallemant, H. G., Mercier, J.-C. C., Carter, N. L., & Ross, J. V. (1980). Rheology of the upper mantle: Inferences from peridotite xenoliths. *Tectonophysics*, *70*(1–2), 85–113. https://doi.org/10.1016/0040-1951(80)90022-0

Bagdassarov, N., Solferino, G., Golabek, G. J., & Schmidt, M. W. (2009). Centrifuge assisted percolation of Fe–S melts in partially molten peridotite: Time constraints for planetary core formation. *Earth and Planetary Science Letters*, *288*(1–2), 84–95. https://doi.org/10.1016/j.epsl.2009.09.010

Ballhaus, C., Bockrath, C., Wohlgemuth-Ueberwasser, C., Laurenz, V., & Berndt, J. (2006). Fractionation of the noble metals by physical processes. *Contributions to Mineralogy and Petrology*, *152*(6), 667–684. https://doi.org/10.1007/s00410-006-0126-z

Bauman, R. P., & Schwaneberg, R. (1994). Interpretation of Bernoulli's equation. *The Physics Teacher*, *32*(8), 478–488. https://doi.org/10.1119/1.2344087

Bockrath, C., Ballhaus, C., & Holzheid, A. (2004). Fractionation of the platinum-group elements during mantle melting. *Science*, *305*(5692), 1951–1953. https://doi.org/10.1126/science.1100160

Cascio, M. Lo, Liang, Y., Shimizu, N., & Hess, P. C. (2008). An experimental study of the grain-scale processes of peridotite melting: Implications for major and trace element distribution during equilibrium and disequilibrium melting. *Contributions to Mineralogy and Petrology*, *156*(1), 87–102. https://doi.org/10.1007/s00410-007-0275-8

Chadam, J., Hoff, D., Merino, E., Ortoleva, P., & Sen, A. (1986). Reactive infiltration instabilities. *IMA Journal of Applied Mathematics (Institute of Mathematics and Its Applications)*, *36*(3), 207–221. https://doi.org/10.1093/imamat/36.3.207

Chen, C., Yao, Z. S., Wang, C. Y. (2022). Partitioning behaviors of cobalt and manganese along diverse melting paths of peridotitic and MORB-like pyroxenitic mantle. *Journal of Petrology*, *63*, 1-22. https://doi.org/10.1093/petrology/egac021

Chowdhury, P., & Dasgupta, R. (2020). Sulfur extraction via carbonated melts from sulfide-bearing mantle lithologies – Implications for deep sulfur cycle and mantle redox. *Geochimica et Cosmochimica Acta, 269,* 376–397. https://doi.org/10.1016/j.gca.2019.11.002

Chung, H. Y., & Mungall, J. E. (2009). Physical constraints on the migration of immiscible fluids through partially molten silicates, with special reference to magmatic sulfide ores. *Earth and Planetary Science Letters*, *286*(1–2), 14–22. https://doi.org/10.1016/j.epsl.2009.05.041

880 Ciazela, J., Koepke, J., Dick, H. J. B., Botcharnikov, R., Muszynski, A., Lazarov, M., et al.
881 (2018). Sulfide enrichment at an oceanic crust-mantle transition zone: Kane Megamullion
882 (23°N, MAR). *Geochimica et Cosmochimica Acta*, *230*, 155–189.
883 https://doi.org/10.1016/j.gca.2018.03.027
884 Connolly, J. A. D., Schmidt, M. W., Solferino, G., & Bagdassarov, N. (2009). Permeability of
885 asthenospheric mantle and melt extraction rates at mid-ocean ridges. *Nature*, *462*(7270), 209–
886 212. https://doi.org/10.1038/nature08517
887 Daines, M. J., & Kohlstedt, D. L. (1994). The transition from porous to channelized flow due to
888 melt/rock reaction during melt migration. *Geophysical Research Letters*, *21*(2), 145–148.
889 https://doi.org/10.1029/93GL03052
890 de Bremond d'Ars, J., Arndt, N. T., & Hallot, E. (2001). Analog experimental insights into the
891 formation of magmatic sulfide deposits. *Earth and Planetary Science Letters*, *186*(3–4), 371–
892 381. https://doi.org/10.1016/S0012-821X(01)00254-0
893 Di Genova, D., Romano, C., Alletti, M., Misiti, V., & Scarlato, P. (2014). The effect of CO_2 and
894 H_2O on Etna and Fondo Riccio (Phlegrean Fields) liquid viscosity, glass transition
895 temperature and heat capacity. *Chemical Geology*, *377*, 72–86.
896 https://doi.org/10.1016/j.chemgeo.2014.04.001
897 Ding, S., & Dasgupta, R. (2017). The fate of sulfide during decompression melting of peridotite
898 – implications for sulfur inventory of the MORB-source depleted upper mantle. *Earth and*
899 *Planetary Science Letters*, *459*, 183–195. https://doi.org/10.1016/j.epsl.2016.11.020
900 Dingwell, D. B. (1996). Volcanic Dilemma--Flow or Blow? *Science*, *273*(5278), 1054–1055.
901 https://doi.org/10.1126/science.273.5278.1054
902 Farquhar, J., Wing, B. A., McKeegan, K. D., Harris, J. W., Cartigny, P., & Thiemens, M. H.
903 (2002). Mass-independent sulfur of inclusions in diamond and sulfur recycling on early Earth.
904 *Science*, *298*(5602), 2369–2372. https://doi.org/10.1126/science.1078617
905 Faul, U. H. (2001). Melt retention and segregation beneath mid-ocean ridges. *Nature*, *410*(6831),
906 920–923. https://doi.org/10.1038/35073556
907 Faul, U. H., & Scott, D. (2006). Grain growth in partially molten olivine aggregates.
908 *Contributions to Mineralogy and Petrology*, *151*(1), 101–111. https://doi.org/10.1007/s00410-
909 005-0048-1

910 Freda, C., Baker, D. R., & Scarlato, P. (2005). Sulfur diffusion in basaltic melts. *Geochimica et*
911 *Cosmochimica Acta*, *69*(21), 5061–5069. https://doi.org/10.1016/j.gca.2005.02.002
912 Ghiorso, M. S., & Sack, R. O. (1995). Chemical mass transfer in magmatic processes IV. A
913 revised and internally consistent thermodynamic model for the interpolation and extrapolation
914 of liquid-solid equilibria in magmatic systems at elevated temperatures and pressures.
915 *Contributions to Mineralogy and Petrology*, *119*(2–3), 197–212.
916 https://doi.org/10.1007/BF00307281
917 Ghiorso, M. S., Hirschmann, M. M., Reiners, P. W., & Kress, V. C. (2002). The pMELTS: A
918 revision of MELTS for improved calculation of phase relations and major element partitioning
919 related to partial melting of the mantle to 3 GPa. *Geochemistry, Geophysics, Geosystems*, *3*(5),
920 1–35. https://doi.org/10.1029/2001gc000217
921 Giordano, D., Russell, J. K., & Dingwell, D. B. (2008). Viscosity of magmatic liquids: A model.
922 *Earth and Planetary Science Letters*, *271*(1–4), 123–134.
923 https://doi.org/10.1016/j.epsl.2008.03.038
924 Griffin, W. L., Begg, G. C., & O'Reilly, S. Y. (2013). Continental-root control on the genesis of
925 magmatic ore deposits. *Nature Geoscience*, *6*(11), 905–910. https://doi.org/10.1038/ngeo1954
926 Heinrich, C. A., & Connolly, J. A. D. (2022). Physical transport of magmatic sulfides promotes
927 copper enrichment in hydrothermal ore fluids. *Geology*, *50*(10), 1101–1105.
928 https://doi.org/10.1130/G50138.1
929 Higgins, M. D. (1998). Origin of Anorthosite by Textural Coarsening: Quantitative
930 Measurements of a Natural Sequence of Textural Development. *Journal of Petrology*, *39*(7),
931 1307–1323. https://doi.org/10.1093/petrology/39.7.1307
932 Higgins, M. D. (2011). Textural coarsening in igneous rocks. *International Geology Review*,
933 *53*(3–4), 354–376. https://doi.org/10.1080/00206814.2010.496177
934 Holwell, D. A., Fiorentini, M. L., Knott, T. R., McDonald, I., Blanks, D. E., Campbell McCuaig,
935 T., & Gorczyk, W. (2022). Mobilisation of deep crustal sulfide melts as a first order control on
936 upper lithospheric metallogeny. *Nature Communications*, *13*(1).
937 https://doi.org/10.1038/s41467-022-28275-y
938 Holzheid, A. (2010). Separation of sulfide melt droplets in sulfur saturated silicate liquids.
939 *Chemical Geology*, *274*(3–4), 127–135. https://doi.org/10.1016/j.chemgeo.2010.03.005

940 Holzheid, A., & Grove, T. L. (2002). Sulfur saturation limits in silicate melts and their
941 implications for core formation scenarios for terrestrial planets. *American Mineralogist*, *87*(2–
942 3), 227–237. https://doi.org/10.2138/am-2002-2-304
943 Holzheid, A., Schmitz, M. D., & Grove, T. L. (2000). Textural equilibria of iron sulfide liquids
944 in partly molten silicate aggregates and their relevance to core formation scenarios. *Journal of*
945 *Geophysical Research: Solid Earth*, *105*(B6), 13555–13567.
946 https://doi.org/10.1029/2000JB900046
947 Honour, V. C., Holness, M. B., Partridge, J. L., & Charlier, B. (2019). Microstructural evolution
948 of silicate immiscible liquids in ferrobasalts. *Contributions to Mineralogy and Petrology*,
949 *174*(9). https://doi.org/10.1007/s00410-019-1610-6
950 Iacono-Marziano, G., Le Vaillant, M., Godel, B. M., Barnes, S. J., & Arbaret, L. (2022). The
951 critical role of magma degassing in sulphide melt mobility and metal enrichment. *Nature*
952 *Communications*, *13*(1). https://doi.org/10.1038/s41467-022-30107-y
953 Jackson, M. D., Blundy, J., & Sparks, R. S. J. (2018). Chemical differentiation, cold storage and
954 remobilization of magma in the Earth's crust. *Nature*, *564*(7736), 405–409.
955 https://doi.org/10.1038/s41586-018-0746-2
956 Karato, S.-I. (1984). Grain-size distribution and rheology of the upper mantle. *Tectonophysics*,
957 *104*(1–2), 155–176. https://doi.org/10.1016/0040-1951(84)90108-2
958 Katz, R. F., Jones, D. W. R., Rudge, J. F., & Keller, T. (2022). Physics of Melt Extraction from
959 the Mantle: Speed and Style. *Annual Review of Earth and Planetary Sciences*, *50*, 507–540.
960 https://doi.org/10.1146/annurev-earth-032320-083704
961 Kelemen, P. B., Shimizu, N., & Salters, V. J. M. (1995). Extraction of mid-ocean-ridge basalt
962 from the upwelling mantle by focused flow of melt in dunite channels. *Nature*, *375*(6534),
963 747–753. https://doi.org/10.1038/375747a0
964 Kress, V., Greene, L. E., Ortiz, M. D., & Mioduszewski, L. (2008). Thermochemistry of sulfide
965 liquids IV: Density measurements and the thermodynamics of O-S-Fe-Ni-Cu liquids at low to
966 moderate pressures. *Contributions to Mineralogy and Petrology*, *156*(6), 785–797.
967 https://doi.org/10.1007/s00410-008-0315-z
968 Lambart, S., Laporte, D., Provost, A., & Schiano, P. (2012). Fate of pyroxenite-derived melts in
969 the peridotitic mantle: Thermodynamic and experimental constraints. *Journal of Petrology*,
970 *53*(3), 451–476. https://doi.org/10.1093/petrology/egr068

971 Lautze, N. C., Sisson, T. W., Mangan, M. T., & Grove, T. L. (2011). Segregating gas from melt:
972 An experimental study of the Ostwald ripening of vapor bubbles in magmas. *Contributions to*
973 *Mineralogy and Petrology*, *161*(2), 331–347. https://doi.org/10.1007/s00410-010-0535-x
974 Lee, C. T. A., & Tang, M. (2020). How to make porphyry copper deposits. *Earth and Planetary*
975 *Science Letters*, *529*, 115868. https://doi.org/10.1016/j.epsl.2019.115868
976 Lee, J. S., & Fung, Y. C. (1969). Stokes flow around a circular cylindrical post confined between
977 two parallel plates. *Journal of Fluid Mechanics*, *37*(4), 657–670.
978 https://doi.org/10.1017/S0022112069000796
979 Liang, Y. (1999). Diffusive dissolution in ternary systems: Analysis with applications to quartz
980 and quartzite dissolution in molten silicates. *Geochimica et Cosmochimica Acta*, *63*(23–24),
981 3983–3995. https://doi.org/10.1016/s0016-7037(99)00203-3
982 Lifshitz, I. M., & Slyozov, V. V. (1961). The kinetics of precipitation from supersaturated solid
983 solutions. *Journal of Physics and Chemistry of Solids*, *19*(1–2), 35–50.
984 https://doi.org/10.1016/0022-3697(61)90054-3
985 Liu, Y., Samaha, N.-T., & Baker, D. R. (2007). Sulfur concentration at sulfide saturation (SCSS)
986 in magmatic silicate melts. *Geochimica et Cosmochimica Acta*, *71*(7), 1783–1799.
987 https://doi.org/10.1016/j.gca.2007.01.004
988 Lorand, J. P., & Luguet, A. (2016). Chalcophile and siderophile elements in Mantle Rocks:
989 Trace elements controlled by trace minerals. *Reviews in Mineralogy and Geochemistry*, *81*(1),
990 441–488. https://doi.org/10.2138/rmg.2016.81.08
991 Lorand, J. P., Alard, O., & Luguet, A. (2010). Platinum-group element micronuggets and
992 refertilization process in Lherz orogenic peridotite (northeastern Pyrenees, France). *Earth and*
993 *Planetary Science Letters*, *289*(1–2), 298–310. https://doi.org/10.1016/j.epsl.2009.11.017
994 Luguet, A., Lorand, J. P., & Seyler, M. (2003). Sulfide petrology and highly siderophile element
995 geochemistry of abyssal peridotites: A coupled study of samples from the Kane Fracture Zone
996 (45°W 23°20N, MARK area, Atlantic Ocean). *Geochimica et Cosmochimica Acta*, *67*(8),
997 1553–1570. https://doi.org/10.1016/S0016-7037(02)01133-X
998 Mallik, A., & Dasgupta, R. (2012). Reaction between MORB-eclogite derived melts and fertile
999 peridotite and generation of ocean island basalts. *Earth and Planetary Science Letters*, *329–*
1000 *330*, 97–108. https://doi.org/10.1016/j.epsl.2012.02.007

1001 Mavrogenes, J. A., & O'Neill, H. S. C. (1999). The relative effects of pressure, temperature and
1002 oxygen fugacity on the solubility of sulfide in mafic magmas. *Geochimica et Cosmochimica*
1003 *Acta*, *63*(7–8), 1173–1180. https://doi.org/10.1016/S0016-7037(98)00289-0
1004 Mckenzie, D. (1984). The generation and compaction of partially molten rock. *Journal of*
1005 *Petrology*, *25*(3), 713–765. https://doi.org/10.1093/petrology/25.3.713
1006 McKenzie, D. (1989). Some remarks on the movement of small melt fractions in the mantle.
1007 *Earth and Planetary Science Letters*, *95*(1–2), 53–72. https://doi.org/10.1016/0012-
1008 821X(89)90167-2
1009 McKenzie, D. (2000). Constraints on melt generation and transport from U-series activity ratios.
1010 *Chemical Geology*, *162*(2), 81–94. https://doi.org/10.1016/S0009-2541(99)00126-6
1011 Médard, E., McCammon, C. A., Barr, J. A., & Grove, T. L. (2008). Oxygen fugacity,
1012 temperature reproducibility, and H_2O contents of nominally anhydrous piston-cylinder
1013 experiments using graphite capsules. *American Mineralogist*, *93*(11–12), 1838–1844.
1014 https://doi.org/10.2138/am.2008.2842
1015 Mei, S., Bai, W., Hiraga, T., & Kohlstedt, D. L. (2002). Influence of melt on the creep behavior
1016 of olivine-basalt aggregates under hydrous conditions. *Earth and Planetary Science Letters*,
1017 *201*(3–4), 491–507. https://doi.org/10.1016/S0012-821X(02)00745-8
1018 Mercier, M., Muro, A. di, Métrich, N., Giordano, D., Belhadj, O., & Mandeville, C. W. (2010).
1019 Spectroscopic analysis (FTIR, Raman) of water in mafic and intermediate glasses and glass
1020 inclusions. *Geochimica et Cosmochimica Acta*, *74*(19), 5641–5656.
1021 https://doi.org/10.1016/j.gca.2010.06.020
1022 Milke, R., Abart, R., Kunze, K., Koch-Müller, M., Schmid, D., & Ulmer, P. (2009). Matrix
1023 rheology effects on reaction rim growth I: Evidence from orthopyroxene rim growth
1024 experiments. *Journal of Metamorphic Geology*, *27*(1), 71–82. https://doi.org/10.1111/j.1525-
1025 1314.2008.00804.x
1026 Miller, K. J., Zhu, W., Montési, L. G. J., & Gaetani, G. A. (2014). Experimental quantification of
1027 permeability of partially molten mantle rock. *Earth and Planetary Science Letters*, *388*, 273–
1028 282. https://doi.org/10.1016/j.epsl.2013.12.003
1029 Mitchell, A. L., & Grove, T. L. (2016). Experiments on melt–rock reaction in the shallow mantle
1030 wedge. *Contributions to Mineralogy and Petrology*, *171*(12). https://doi.org/10.1007/s00410-
1031 016-1312-2

1032 Morgan, Z., & Liang, Y. (2003). An experimental and numerical study of the kinetics of
1033 harzburgite reactive dissolution with applications to dunite dike formation. *Earth and*
1034 *Planetary Science Letters*, *214*(1–2), 59–74. https://doi.org/10.1016/S0012-821X(03)00375-3
1035 Morgan, Z., & Liang, Y. (2005). An experimental study of the kinetics of lherzolite reactive
1036 dissolution with applications to melt channel formation. *Contributions to Mineralogy and*
1037 *Petrology*, *150*(4), 369–385. https://doi.org/10.1007/s00410-005-0033-8
1038 Mungall, J. E., Brenan, J. M., Godel, B., Barnes, S. J., & Gaillard, F. (2015). Transport of metals
1039 and sulphur in magmas by flotation of sulphide melt on vapour bubbles. *Nature Geoscience*,
1040 *8*(3), 216–219. https://doi.org/10.1038/ngeo2373
1041 Mungall, J. E. (2002). Empirical models relating viscosity and tracer diffusion in magmatic
1042 silicate melts. *Geochimica et Cosmochimica Acta*, *66*(1), 125–143.
1043 https://doi.org/10.1016/S0016-7037(01)00736-0
1044 Mungall, J. E., & Brenan, J. M. (2014). Partitioning of platinum-group elements and Au between
1045 sulfide liquid and basalt and the origins of mantle-crust fractionation of the chalcophile
1046 elements. *Geochimica et Cosmochimica Acta*, *125*, 265–289.
1047 https://doi.org/10.1016/j.gca.2013.10.002
1048 Niu, Y. (2004). Bulk-rock major and trace element compositions of abyssal peridotites:
1049 Implications for mantle melting, melt extraction and post-melting processes beneath Mid-
1050 Ocean ridges. *Journal of Petrology*, *45*(12), 2423–2458.
1051 https://doi.org/10.1093/petrology/egh068
1052 Pan, F., Zhang, H., He, X., Harris, N., Dai, H.K., Xiong, Q., Luo, B., Liu, D., Kusky, T., &
1053 Sadiq, I. (2023). Lithosphere tearing and foundering during continental subduction: insights
1054 from Oligocene-Miocene magmatism in southern Tibet. *GSA Bulletin*,
1055 https://doi.org/10.1130/B36746.1
1056 Patten, C., Barnes, S. J., Mathez, E. A., & Jenner, F. E. (2013). Partition coefficients of
1057 chalcophile elements between sulfide and silicate melts and the early crystallization history of
1058 sulfide liquid: LA-ICP-MS analysis of MORB sulfide droplets. *Chemical Geology*, *358*, 170–
1059 188. https://doi.org/10.1016/j.chemgeo.2013.08.040
1060 Pec, M., Holtzman, B. K., Zimmerman, M. E., & Kohlstedt, D. L. (2015). Reaction infiltration
1061 instabilities in experiments on partially molten mantle rocks. *Geology*, *43*(7), 575–578.
1062 https://doi.org/10.1130/G36611.1

1063 Pec, M., Holtzman, B. K., Zimmerman, M. E., & Kohlstedt, D. L. (2017). Reaction infiltration
1064 instabilities in mantle rocks: An experimental investigation. *Journal of Petrology*, *58*(5), 979–
1065 1003. https://doi.org/10.1093/petrology/egx043
1066 Pin, J., France, L., Lambart, S., & Reisberg, L. (2022). Thermodynamic modeling of melt
1067 addition to peridotite: Implications for the refertilization of the non-cratonic continental
1068 mantle lithosphere. *Chemical Geology*, *609*, 121050.
1069 https://doi.org/10.1016/j.chemgeo.2022.121050
1070 Rees Jones, D. W., & Rudge, J. F. (2020). Fast magma ascent, revised estimates from the
1071 deglaciation of Iceland. *Earth and Planetary Science Letters*, *542*, 116324.
1072 https://doi.org/10.1016/j.epsl.2020.116324
1073 Robertson, J. C., Barnes, S. J., & Le Vaillant, M. (2016). Dynamics of magmatic sulphide
1074 droplets during transport in silicate melts and implications for magmatic sulphide ore
1075 formation. *Journal of Petrology*, *56*(12), 2445–2472. https://doi.org/10.1093/petrology/egv078
1076 Rubin, K. H., van der Zander, I., Smith, M. C., & Bergmanis, E. C. (2005). Minimum speed limit
1077 for ocean ridge magmatism from ^{210}Pb–^{226}Ra–^{230}Th disequilibria. *Nature*, *437*(7058), 534–
1078 538. https://doi.org/10.1038/nature03993
1079 Shaw, C. S. J., Lebert, B. S., & Woodland, A. B. (2018). Thermodynamic modelling of mantle-
1080 melt interaction evidenced by veined wehrlite xenoliths from the Rockeskyllerkopf Volcanic
1081 Complex, West Eifel volcanic field, Germany. *Journal of Petrology*, *59*(1), 59–86.
1082 https://doi.org/10.1093/petrology/egy018
1083 Smith, P. M., & Asimow, P. D. (2005). Adiabat-1ph: A new public front-end to the MELTS,
1084 pMELTS, and pHMELTS models. *Geochemistry, Geophysics, Geosystems*, *6*(2), 1–8.
1085 https://doi.org/10.1029/2004GC000816
1086 Smythe, D. J., Wood, B. J., & Kiseeva, E. S. (2017). The S content of silicate melts at sulfide
1087 saturation: New experiments and a model incorporating the effects of sulfide composition.
1088 *American Mineralogist*, *102*(4), 795–803. https://doi.org/10.2138/am-2017-5800CCBY
1089 Spiegelman, M., Kelemen, P. B., & Aharonov, E. (2001). Causes and consequences of flow
1090 organization during melt transport: The reaction infiltration instability in compactible media.
1091 *Journal of Geophysical Research: Solid Earth*, *106*(B2), 2061–2077.
1092 https://doi.org/10.1029/2000JB900240

1093 Sun, W. (2007). Kinetics for coarsening co-controlled by diffusion and a reversible interface
1094 reaction. *Acta Materialia*, *55*(1), 313–320. https://doi.org/10.1016/j.actamat.2006.07.045
1095 Sundberg, M., Hirth, G., & Kelemen, P. B. (2010). Trapped melt in the Josephine peridotite:
1096 Implications for permeability and melt extraction in the upper mantle. *Journal of Petrology*,
1097 *51*(1–2), 185–200. https://doi.org/10.1093/petrology/egp089
1098 Sweeney, S. M., & Martin, C. L. (2003). Pore size distributions calculated from 3-D images of
1099 DEM-simulated powder compacts. *Acta Materialia*, *51*(12), 3635–3649.
1100 https://doi.org/10.1016/S1359-6454(03)00183-6
1101 von Bargen, N., & Waff, H. S. (1986). Permeabilities, interfacial areas and curvatures of partially
1102 molten systems: Results of numerical computations of equilibrium microstructures. *Journal of*
1103 *Geophysical Research*, *91*(B9), 9261–9276. https://doi.org/10.1029/JB091iB09p09261
1104 Wagner, C. (1961). Theorie der Alterung von Niederschlägen durch Umlösen (Ostwald-
1105 Reifung). *Zeitschrift Für Elektrochemie, Berichte Der Bunsengesellschaft Für Physikalische*
1106 *Chemie*, *65*(7–8), 581–591. https://doi.org/10.1002/bbpc.19610650704
1107 Wang, C., Liang, Y., Xu, W., & Dygert, N. (2013). Effect of melt composition on basalt and
1108 peridotite interaction: Laboratory dissolution experiments with applications to mineral
1109 compositional variations in mantle xenoliths from the North China Craton. *Contributions to*
1110 *Mineralogy and Petrology*, *166*(5), 1469–1488. https://doi.org/10.1007/s00410-013-0938-6
1111 Wang, C., Liang, Y., Dygert, N., & Xu, W. (2016). Formation of orthopyroxenite by reaction
1112 between peridotite and hydrous basaltic melt: an experimental study. *Contributions to*
1113 *Mineralogy and Petrology*, *171*(8–9). https://doi.org/10.1007/s00410-016-1287-z
1114 Wang, C., Lo Cascio, M., Liang, Y., & Xu, W. (2020). An experimental study of peridotite
1115 dissolution in eclogite-derived melts: Implications for styles of melt-rock interaction in
1116 lithospheric mantle beneath the North China Craton. *Geochimica et Cosmochimica Acta*, *278*,
1117 157–176. https://doi.org/10.1016/j.gca.2019.09.022
1118 Wang, J., Xiong, X., Zhang, L., & Takahashi, E. (2020). Element loss to platinum capsules in
1119 high-temperature-pressure experiments. *American Mineralogist*, *105*(10), 1593–1597.
1120 https://doi.org/10.2138/am-2020-7580
1121 Wang, K.-L., O'Reilly, S. Y., Griffin, W. L., Pearson, N. J., & Zhang, M. (2009). Sulfides in
1122 mantle peridotites from Penghu Islands, Taiwan: Melt percolation, PGE fractionation, and the

lithospheric evolution of the South China block. *Geochimica et Cosmochimica Acta*, *73*(15), 4531–4557. https://doi.org/10.1016/j.gca.2009.04.030

Wang, Z. J., & Jin, Z. (2020). Reaction Infiltration Instabilities in Partially Molten Peridotite and Implications for Driving the Transport of Sulfide Liquid. *Journal of Earth Science*, *31*(3), 447–455. https://doi.org/10.1007/s12583-020-1301-2

Wang, Z. J., Jin, Z., Mungall, J. E., & Xiao, X. (2020). Transport of coexisting Ni-Cu sulfide liquid and silicate melt in partially molten peridotite. *Earth and Planetary Science Letters*, *536*, 116162. https://doi.org/10.1016/j.epsl.2020.116162

Yao, Z. S., & Mungall, J. E. (2021). Kinetic controls on the sulfide mineralization of komatiite-associated Ni-Cu-(PGE) deposits. *Geochimica et Cosmochimica Acta*, *305*, 185–211. https://doi.org/10.1016/j.gca.2021.05.009

Yao, Z. S., Qin, K. Z., & Xue, S. C. (2017). Kinetic processes for plastic deformation of olivine in the Poyi ultramafic intrusion, NW China: Insights from the textural analysis of a ~ 1700 m fully cored succession. *Lithos*, *284–285*, 462–476. https://doi.org/10.1016/j.lithos.2017.05.002

Yao, Z. S., & Mungall, J. E. (2020). Flotation mechanism of sulphide melt on vapour bubbles in partially molten magmatic systems. *Earth and Planetary Science Letters*, *542*, 116298. https://doi.org/10.1016/j.epsl.2020.116298

Yao, Z. S., Qin, K. Z., & Mungall, J. E. (2018). Tectonic controls on Ni and Cu contents of primary mantle-derived magmas for the formation of magmatic sulfide deposits. *American Mineralogist*, *103*(10), 1545–1567. https://doi.org/10.2138/am-2018-6392

Yao, Z. S., Mungall, J. E., & Qin, K. Z. (2019). A preliminary model for the migration of sulfide droplets in a magmatic conduit and the significance of volatiles. *Journal of Petrology*, *60*(12), 2281–2316. https://doi.org/10.1093/petrology/egaa005

Yao, Z. S., Mungall, J. E., & Jenkins, M. C. (2021). The Rustenburg Layered Suite formed as a stack of mush with transient magma chambers. *Nature Communications*, *12*(1), 1–14. https://doi.org/10.1038/s41467-020-20778-w

Yoshino, T., & Watson, E. B. (2005). Growth kinetics of FeS melt in partially molten peridotite: An analog for core-forming processes. *Earth and Planetary Science Letters*, *235*(1–2), 453–468. https://doi.org/10.1016/j.epsl.2005.04.021

Yoshino, T., Walter, M. J., & Katsura, T. (2003). Core formation in planetesimals triggered by permeable flow. *Nature*, *422*(6928), 154–157. https://doi.org/10.1038/nature01459

Yoshino, T., Walter, M. J., & Katsura, T. (2004). Connectivity of molten Fe alloy in peridotite based on in situ electrical conductivity measurements: Implications for core formation in terrestrial planets. *Earth and Planetary Science Letters*, *222*(2), 625–643. https://doi.org/10.1016/j.epsl.2004.03.010

Yoshino, T., Laumonier, M., McIsaac, E., & Katsura, T. (2010). Electrical conductivity of basaltic and carbonatite melt-bearing peridotites at high pressures: Implications for melt distribution and melt fraction in the upper mantle. *Earth and Planetary Science Letters*, *295*(3–4), 593–602. https://doi.org/10.1016/j.epsl.2010.04.050

Zhang, Y. (2015). Toward a quantitative model for the formation of gravitational magmatic sulfide deposits. *Chemical Geology*, *391*, 56–73. https://doi.org/10.1016/j.chemgeo.2014.10.025

Zhang, Y., Walker, D., & Lesher, C. E. (1989). Diffusive crystal dissolution. *Contributions to Mineralogy and Petrology*, *102*(4), 492–513. https://doi.org/10.1007/BF00371090

Zhang, Y., Ni, H., & Chen, Y. (2010). Diffusion data in silicate melts. *Reviews in Mineralogy and Geochemistry*, *72*(1), 311–408. https://doi.org/10.2138/rmg.2010.72.8

Zhao, Y., Liu, S. A., Xue, C., & Li, M. L. (2022). Copper isotope evidence for a Cu-rich mantle source of the world-class Jinchuan magmatic Ni-Cu deposit. *American Mineralogist*, *107*(4), 673–683. https://doi.org/10.2138/am-2021-7911

Zhu, W., Gaetani, G. A., Fusseis, F., Montési, L. G. J., & de Carlo, F. (2011). Microtomography of partially molten rocks: Three-dimensional melt distribution in mantle peridotite. *Science*, *332*(6025), 88–91. https://doi.org/10.1126/science.1202221

Figure 1. Back-scattered electron images (BSE) of sections from experiments PC520 (a) (annealing time ~ 12 h) and PC545 (b) (annealing time ~ 72 h) under the conditions of 1.5 GPa and 1,250 ℃. Dashed red and blue lines respectively denote the original and current interfaces between the melt source and peridotite before and after the melt-rock reaction. The dashed yellow line marks the top of the Opx-rich reaction layer. The position where the melt fraction at the top of the melt source decreases below 10 – 15 vol% is set as the possible lower boundary of ORL for the measurement (the dashed white line), which is approximately consistent with the original interface between the melt source and peridotite at short annealing time (< 48 h). The width of these quenched cracks needs to be subtracted. The specimen setup of these experiments

is shown as the inset in the left lower part. Mineral abbreviations: Ol-olivine; Opx-orthopyroxene; SM-silicate melt; SL-sulfide liquid.

Figure 2. Microstructures of the interface of melt-rock reaction in experiments PC545 (72 h, 1,250 ℃) (a), PC528 (48 h, 1,250 ℃) (b, c), and PC527 (12 h, 1,300 ℃) (d). Detailed microstructure of the distribution of sulfide droplets and silicate melt in the partially molten peridotite is displayed in (c). Symbols are the same as in Figure 1. Mineral abbreviations: Ol-olivine; Opx-orthopyroxene; SM-silicate melt; SL-sulfide liquid. Note that some huge Opx grains are present in the Opx-rich reaction layer of experiment PC527 with high reaction temperature, potentially leading to the destruction of the layer.

Figure 3. Plots of thicknesses of Opx-rich reaction layers (ORL) (a) and dissolution distance (b) as a function of the square root of run time. The lines show the best fit for these data. *k* is the diffusive dissolution or growth rate which is the slope of the linear regression line. The grey symbols and lines denoted as 3 and 4 are from Morgan & Liang (2005), and those denoted as 1, 2, 5, and 6 are from C. Wang et al. (2020). The blue symbols and lines denoted as 7 are from this study. Note that the dissolution distance and the thickness of ORL may be slightly underestimated and overestimated, respectively, due to the possible gravitational settling of minerals in our experiments.

Figure 4. Plots of melt fraction (a) and grain size of silicate minerals (b) as a function of the square root of run time in the partially molten peridotite from our experiments.

Figure 5. Plots of grain size (μm) of sulfide droplets weighted by the area (a and c) and the area fraction of sulfide droplets (b and d) as a function of the square root of run time in the melt source (lower part) and partially molten peridotite (upper part). Inset in (a) shows the relationship between the number density of sulfide droplets in the melt source and the square root of run time. All symbols representing samples are the same as those in (c).

Figure 6. Plots (a-g) of measured oxide abundance (in wt.%) and Mg# in olivine as a function of distance (in μm) away from the melt-rock interface. The compositional variations of MgO, Mg#, and FeO are also simulated thermodynamically as a function of the melt-peridotite ratio in (h). These measured compositions of olivine approaching to the interface are roughly consistent with

those results simulated thermodynamically (the gray shadow region in h), when the melt-rock ratio ranges from 1 to 1.5 (Table S6). At low pressure (PC559, 0.5 GPa), the compositions of olivine recrystallized in the melt source during the melt-rock reaction are present as PC559-Lower (hollow black square). The compositions of olivine grains within the low-temperature hot-press experiment (PC537) were almost constant across the partially molten peridotite region and thus can be used as the reference line (purple dotted lines) to show the composition variations of olivine in those high-temperature reaction experiments. The gray shadow regions in (a)-(g) denote the region that has a vigorous melt-peridotite reaction, whose width is not in accordance with the actual distance.

Figure 7. Plots (a-g) of oxide abundance (in wt.%) and Mg# in clinopyroxene as a function of distance (in μm) away from the melt-rock interface. The compositional variations of MgO, Al_2O_3, and CaO are also simulated thermodynamically as a function of the melt-peridotite ratio in (h). The legends are the same as in Figure 6.

Figure 8. Plots of oxide abundance (in wt.%) (a-e), sulfur content (f), and viscosity (μ_m) (g) of silicate melt versus the run time in melt-rock interface and lower melt source of these reaction experiments. The ranges of composition variations of SiO_2, Al_2O_3, FeO, CaO, and MgO simulated thermodynamically are denoted as shadow gray regions in (a)-(e) when the melt-peridotite ratio varies from 1 to 1.5. The shadow gray region in (f) is the calculated SCSS based on the models from Chowdhury & Dasgupta (2020) and Smythe et al. (2017), and the SCSS value at t = 0 is calculated by using the compositions of starting materials under conditions of 1,250 ℃ and 1.5 GPa. The composition of sulfides in starting materials (Table S3) was used to estimate the SCSS in experiments PC559 and PC560. Produced phase proportions of different silicate minerals during the melt-rock reaction are simulated thermodynamically as a function of melt-peridotite ratio in (h). A lower melt viscosity (~ 0.25 Pa·s) of the carbonate-bearing experiment (PC560) is roughly estimated by using a model from Di Genova et al. (2014) considering the effect of CO_3^{2-} (~ 2 wt.%) and denoted as a hollow inverted triangle in (g). Cpx-clinopyroxene, Opx-orthopyroxene.

Figure 9. Normalized 3D size distributions of sulfide droplets in melt source. The size of sulfide droplets (r) and frequency (f) have been normalized to average size (r^*) and maximum frequency (f_{max}), respectively.

Figure 10. Schematic map illustrating the fluid flow around a circular cylindrical particle confined by two parallel flat plates (a), the dimensionless coefficients f_D is shown as a function of the R/r_s ratio (b) (modified from Lee & Fung, 1969), and the extrusion and entrainment of large (left side) and small (right side) sulfide droplets driven by focused melt flow (c). In (a), the two parallel flat plates and a circular cylindrical particle are considered as the walls of the pore throat/melt channel and sulfide droplet, respectively.

Figure 11. Plots of the radius (r_s) of initial undeformed sulfide droplets that could extrude the pore throat as a function of the porosity (Φ) of the partially molten mantle. The relationship between r_s and Φ is divided into three parts according to the relative size of sulfide droplets' radius (r_s) and the pore throat's minimum constriction (R). The description of these three regions can be found in the main text.

Table 1. Experimental conditions and the observed lithologies.

Figure 1.

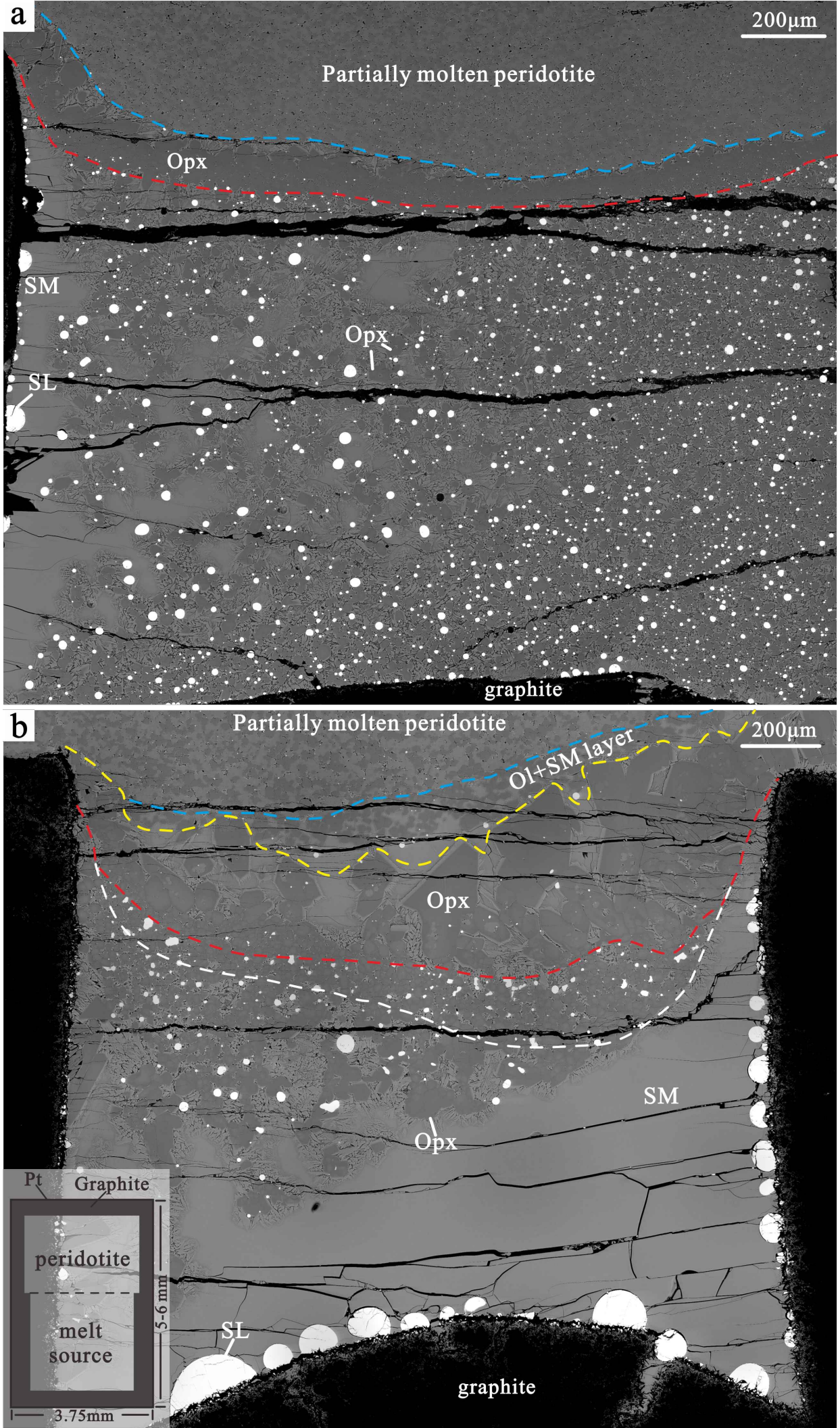
a
200μm
Partially molten peridotite
Opx
SM
Opx
SL
graphite
b
Partially molten peridotite
200μm
Ol+SM layer
Opx
SM
Opx
Pt
Graphite
peridotite
melt
source
5-6 mm
3.75mm
SL
graphite

Figure 2.

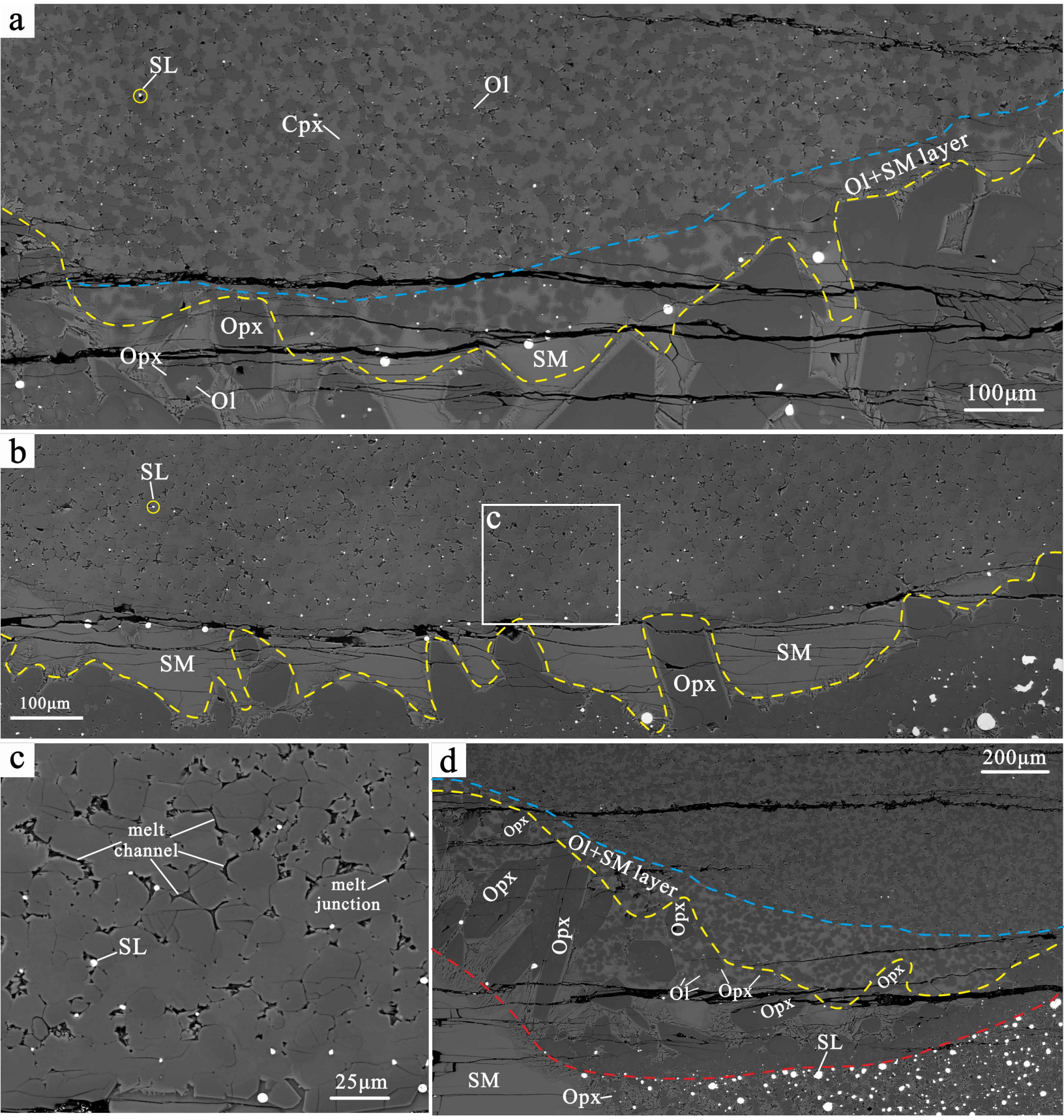
a
SL
Ol
Cpx
Ol+SM layer
Opx
Opx
SM
Ol
100μm
b
SL
c
SM
SM
Opx
100μm
c
melt
channel
melt
junction
SL
25μm
d
200μm
Opx
Ol+SM layer
Opx
Opx
Opx
Ol
Opx
Opx
Opx
SL
SM
Opx

Figure 3.

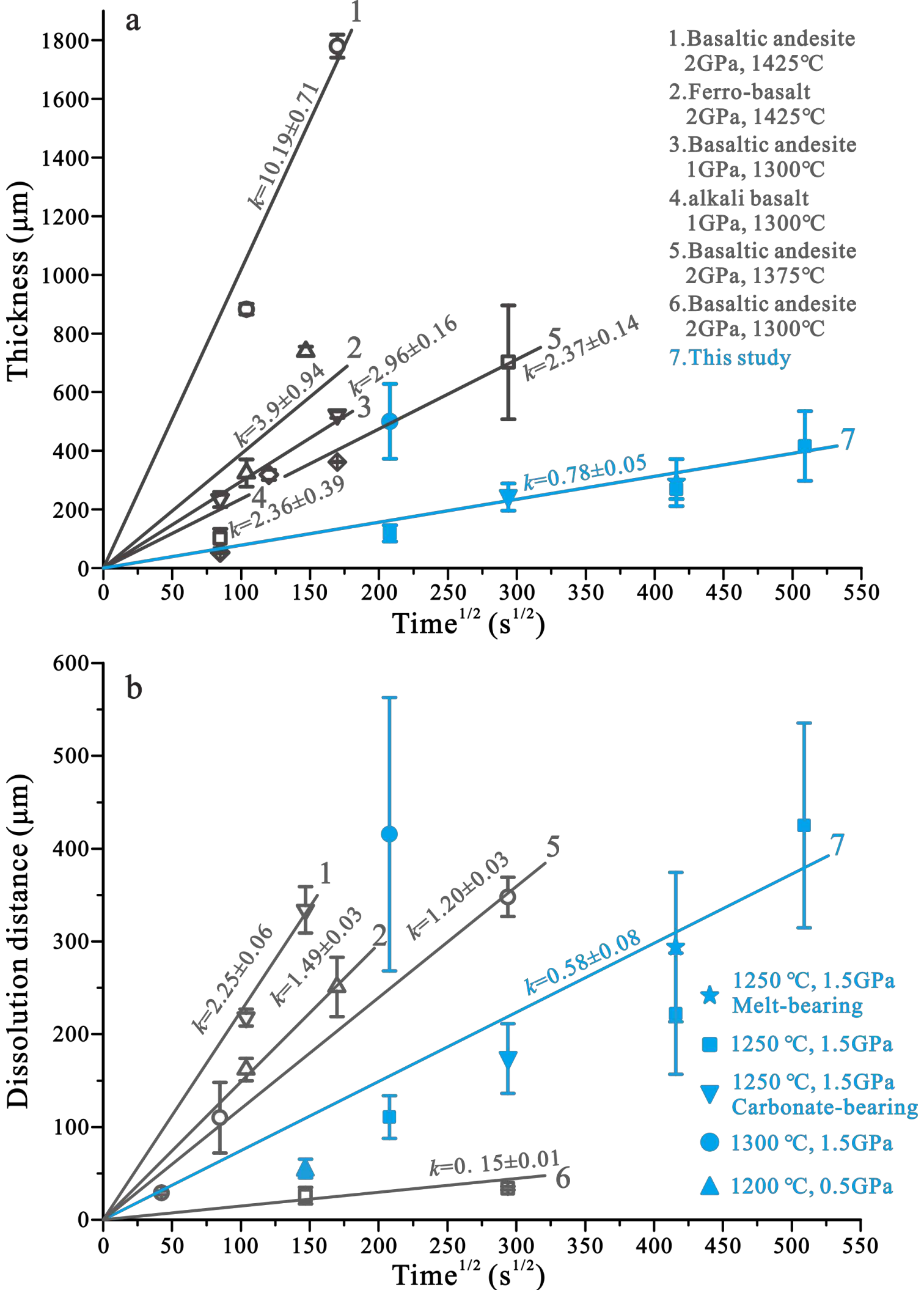
a
Thickness (μm)
Time$^{1/2}$ (s$^{1/2}$)
1.Basaltic andesite 2GPa, 1425℃
2.Ferro-basalt 2GPa, 1425℃
3.Basaltic andesite 1GPa, 1300℃
4.alkali basalt 1GPa, 1300℃
5.Basaltic andesite 2GPa, 1375℃
6.Basaltic andesite 2GPa, 1300℃
7.This study
k=10.19±0.71
k=3.9±0.94
k=2.96±0.16
k=2.37±0.14
k=2.36±0.39
k=0.78±0.05
b
Dissolution distance (μm)
Time$^{1/2}$ (s$^{1/2}$)
k=2.25±0.06
k=1.49±0.03
k=1.20±0.03
k=0.58±0.08
k=0. 15±0.01
1250 ℃, 1.5GPa Melt-bearing
1250 ℃, 1.5GPa
1250 ℃, 1.5GPa Carbonate-bearing
1300 ℃, 1.5GPa
1200 ℃, 0.5GPa

Figure 4.

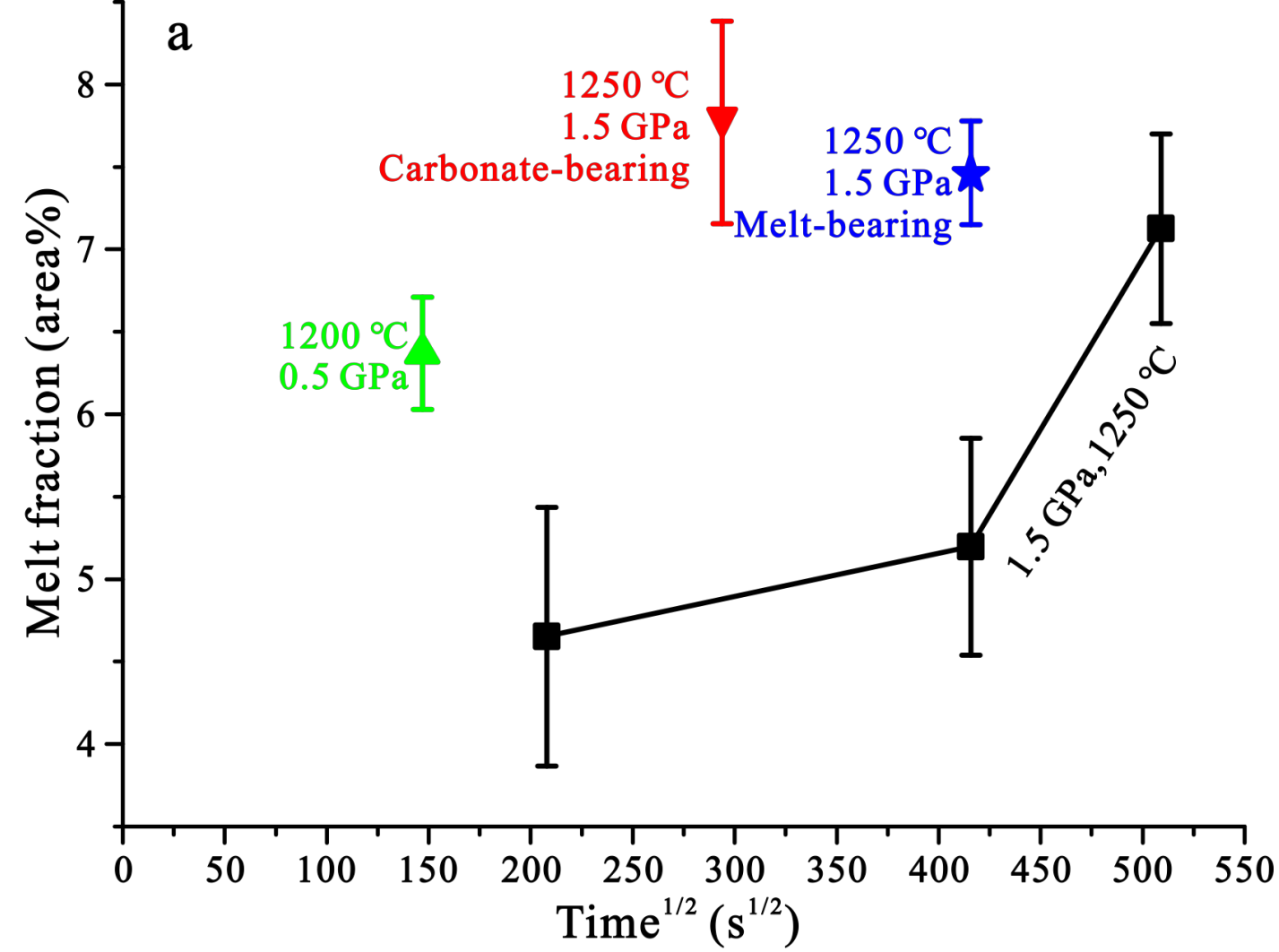
a
1250 ℃
1.5 GPa
Carbonate-bearing
1250 ℃
1.5 GPa
Melt-bearing
1200 ℃
0.5 GPa
1.5 GPa,1250 ℃
Melt fraction (area%)
Time^1/2 (s^1/2)

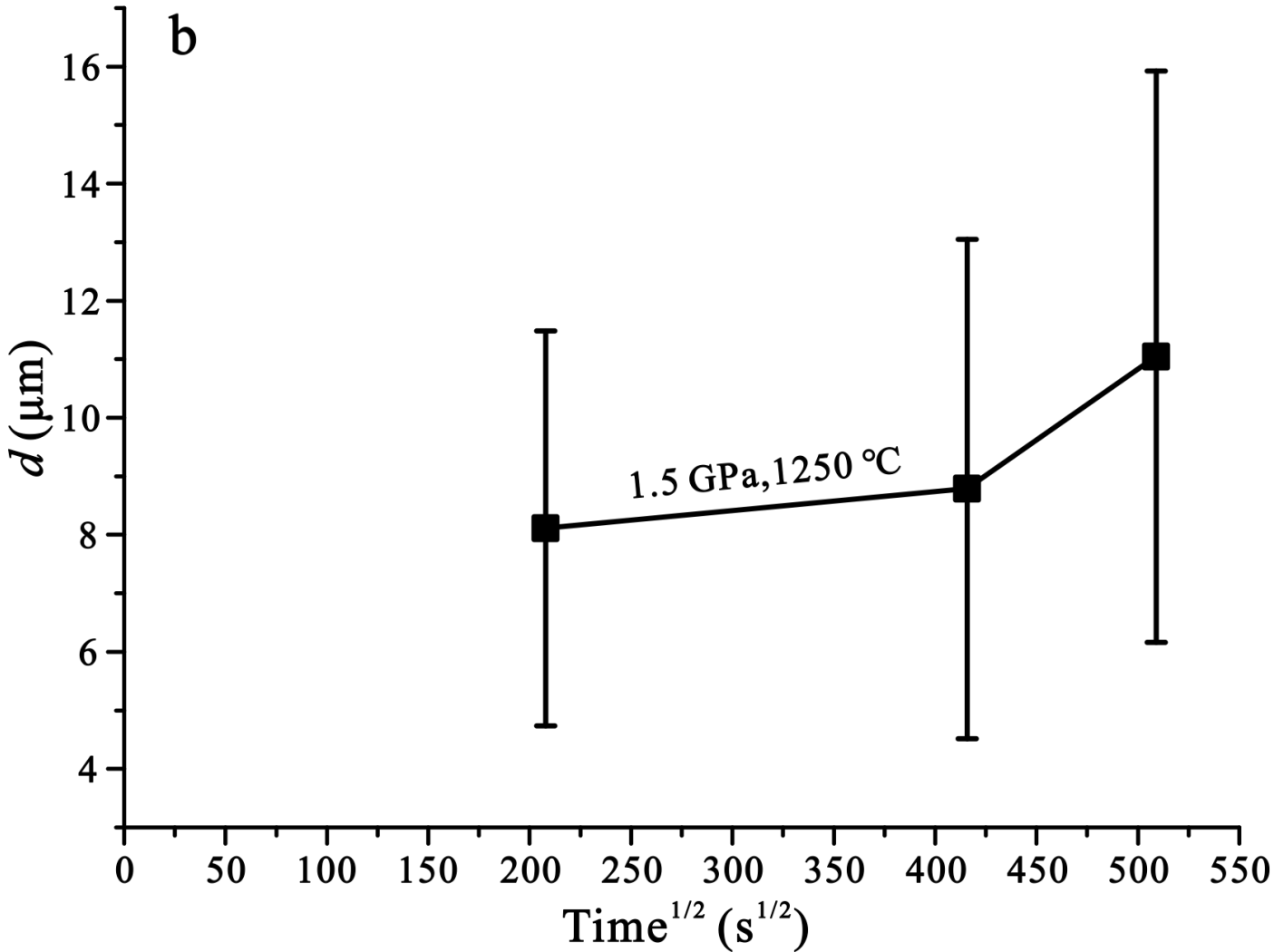
b
1.5 GPa,1250 ℃
d (μm)
Time^1/2 (s^1/2)

Figure 5.

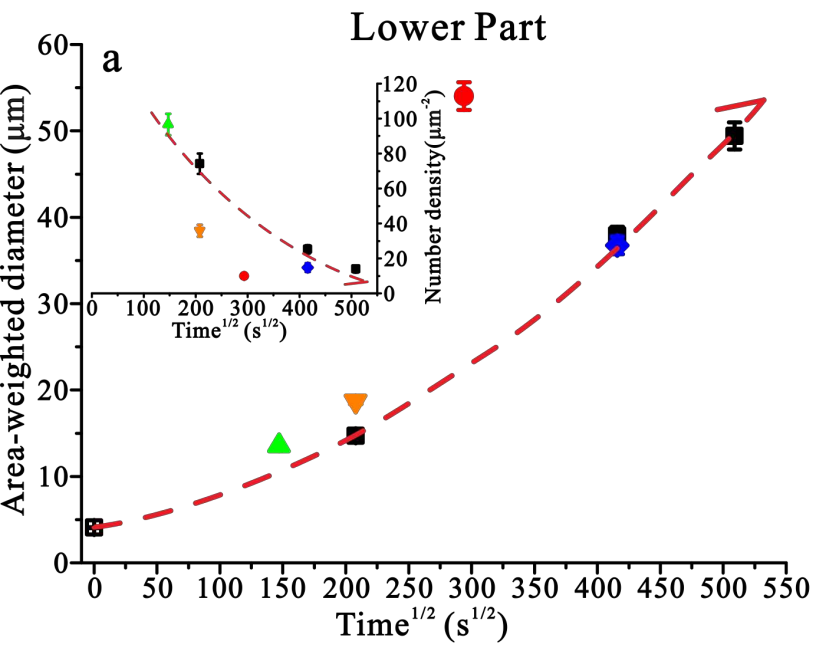
Lower Part
a
Area-weighted diameter (μm)
Time$^{1/2}$ (s$^{1/2}$)
Number density(μm^{-2})
Time$^{1/2}$ (s$^{1/2}$)

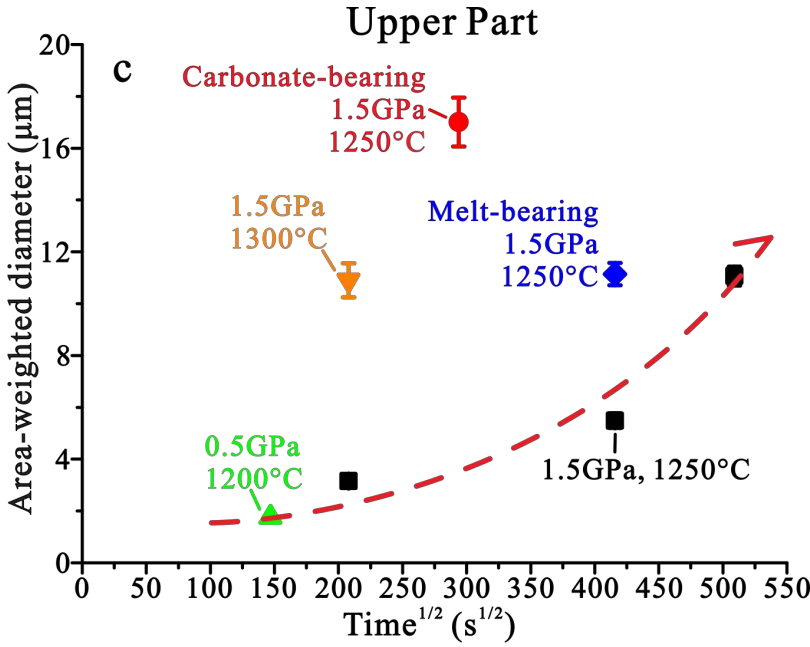
Upper Part
c
Carbonate-bearing
1.5GPa
1250°C
1.5GPa
1300°C
Melt-bearing
1.5GPa
1250°C
0.5GPa
1200°C
1.5GPa, 1250°C
Area-weighted diameter (μm)
Time$^{1/2}$ (s$^{1/2}$)

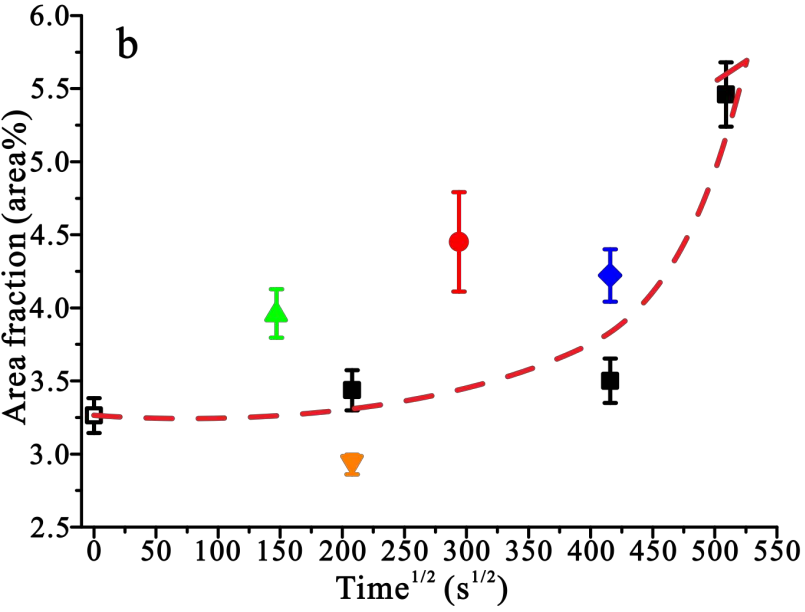
b
Area fraction (area%)
Time$^{1/2}$ (s$^{1/2}$)

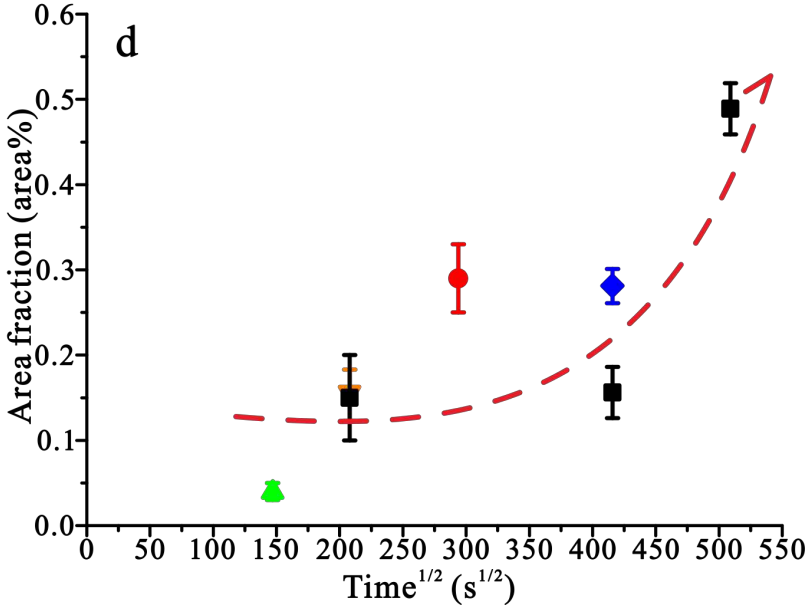
d
Area fraction (area%)
Time$^{1/2}$ (s$^{1/2}$)

Figure 6.

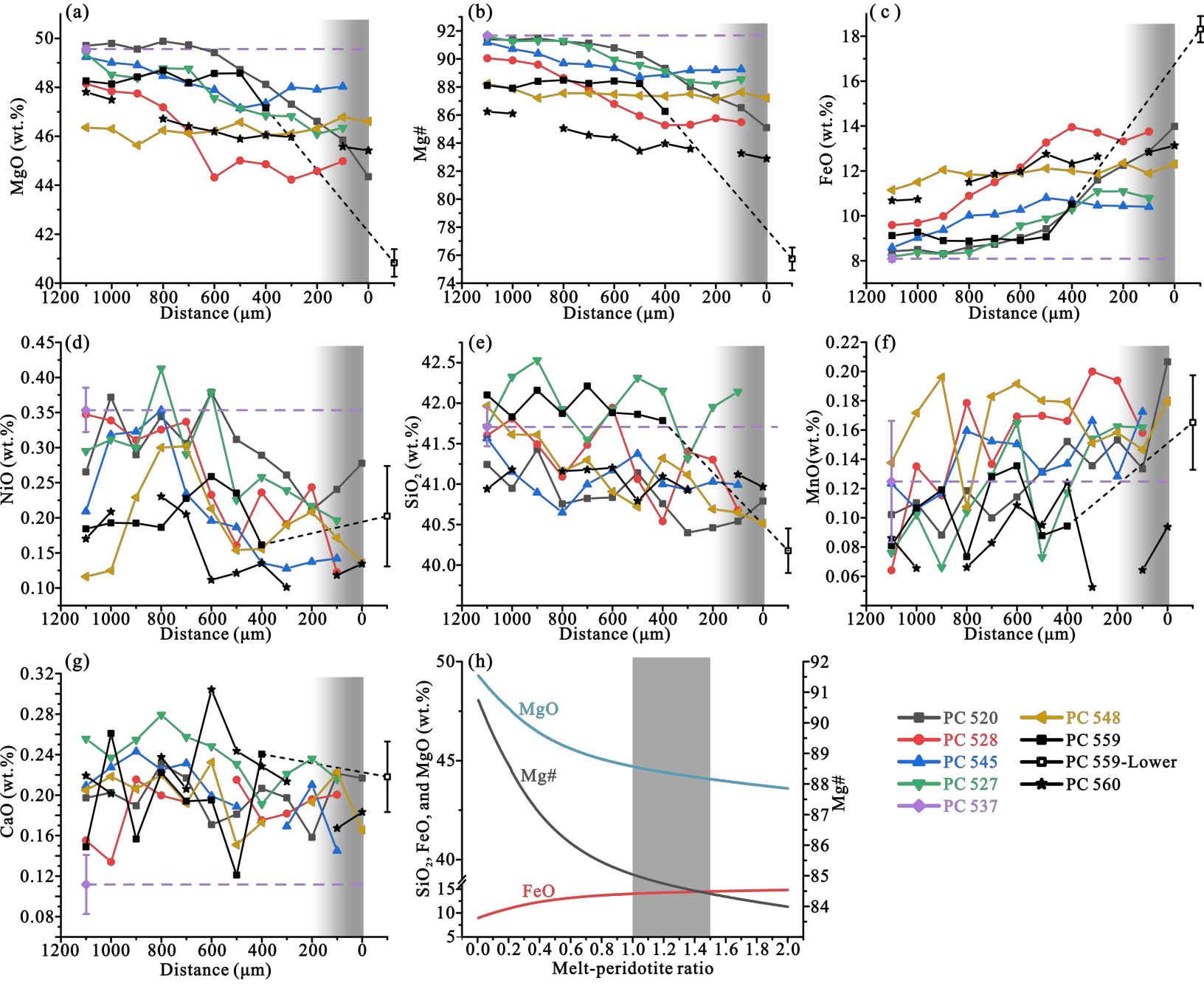
(a)
MgO (wt.%)
Distance (μm)
(b)
Mg#
Distance (μm)
(c)
FeO (wt.%)
Distance (μm)
(d)
NiO (wt.%)
Distance (μm)
(e)
SiO2 (wt.%)
Distance (μm)
(f)
MnO(wt.%)
Distance (μm)
(g)
CaO (wt.%)
Distance (μm)
(h)
SiO2, FeO, and MgO (wt.%)
Mg#
MgO
Mg#
FeO
Melt-peridotite ratio
PC 520
PC 528
PC 545
PC 527
PC 537
PC 548
PC 559
PC 559-Lower
PC 560

Figure 7.

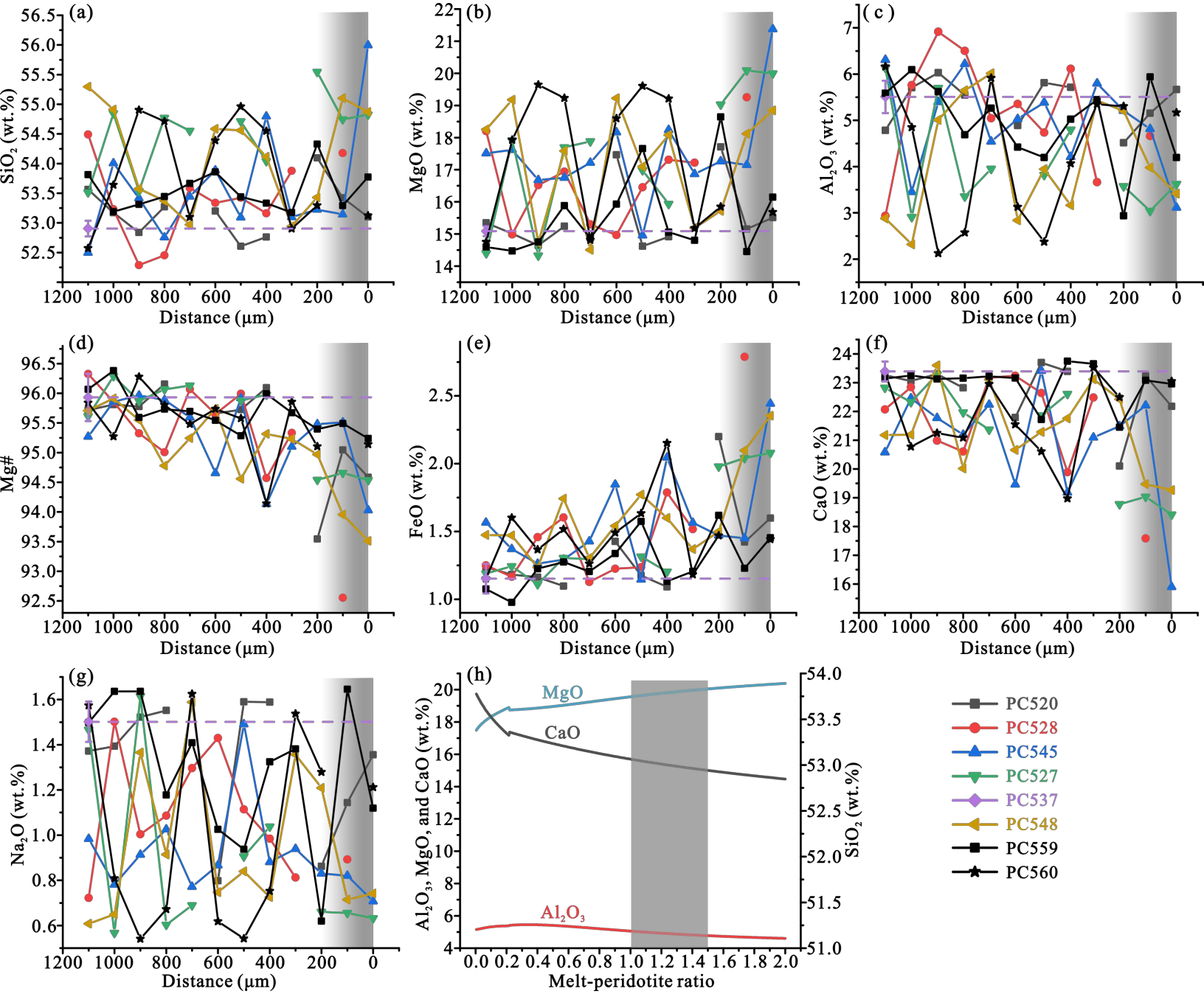
(a)
SiO2 (wt.%)
(b)
MgO (wt.%)
(c)
Al2O3 (wt.%)
(d)
Mg#
(e)
FeO (wt.%)
(f)
CaO (wt.%)
(g)
Na2O (wt.%)
(h)
Al2O3, MgO, and CaO (wt.%)
SiO2 (wt.%)
MgO
CaO
Al2O3
Melt-peridotite ratio
Distance (μm)
PC520
PC528
PC545
PC527
PC537
PC548
PC559
PC560

Figure 8.

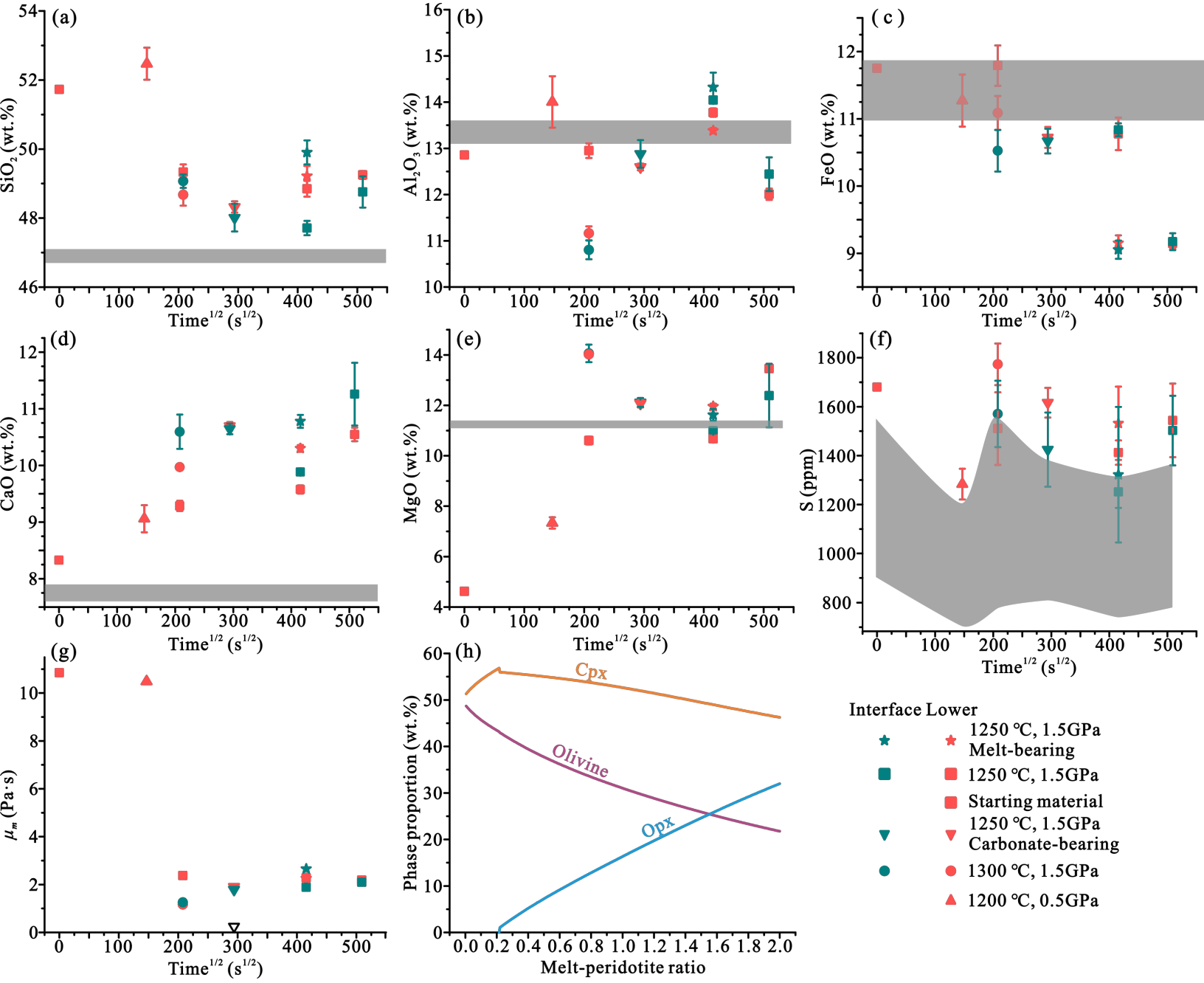
(a)
SiO2 (wt.%)
Time1/2 (s1/2)
(b)
Al2O3 (wt.%)
Time1/2 (s1/2)
(c)
FeO (wt.%)
Time1/2 (s1/2)
(d)
CaO (wt.%)
Time1/2 (s1/2)
(e)
MgO (wt.%)
Time1/2 (s1/2)
(f)
S (ppm)
Time1/2 (s1/2)
(g)
μm (Pa·s)
Time1/2 (s1/2)
(h)
Phase proportion (wt.%)
Melt-peridotite ratio
Cpx
Olivine
Opx
Interface Lower
1250 ℃, 1.5GPa Melt-bearing
1250 ℃, 1.5GPa Starting material
1250 ℃, 1.5GPa Carbonate-bearing
1300 ℃, 1.5GPa
1200 ℃, 0.5GPa

Figure 9.

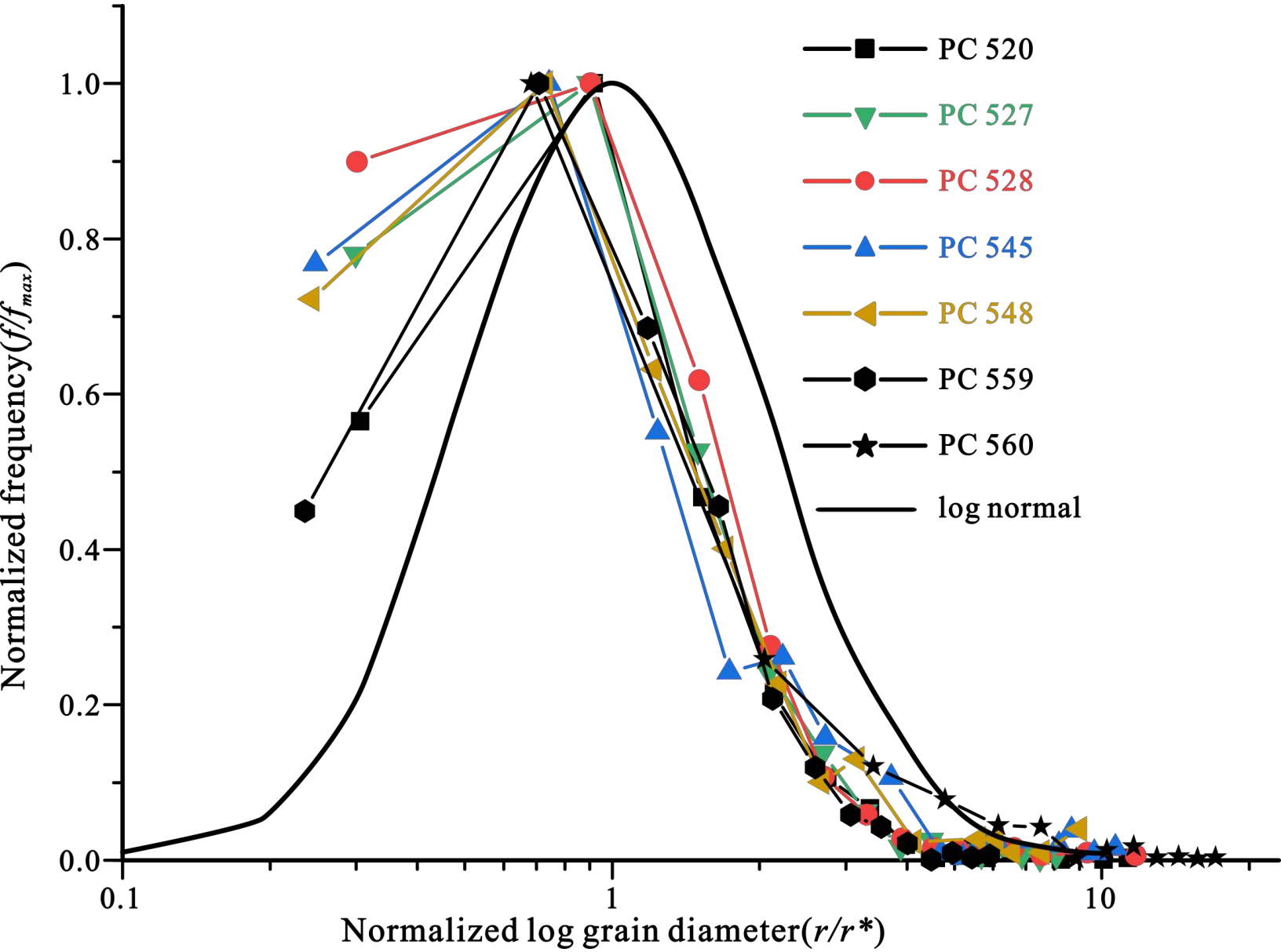
PC 520
PC 527
PC 528
PC 545
PC 548
PC 559
PC 560
log normal
Normalized frequency(f/f_max)
Normalized log grain diameter(r/r*)
1.0
0.8
0.6
0.4
0.2
0.0
0.1
1
10

Figure 10.

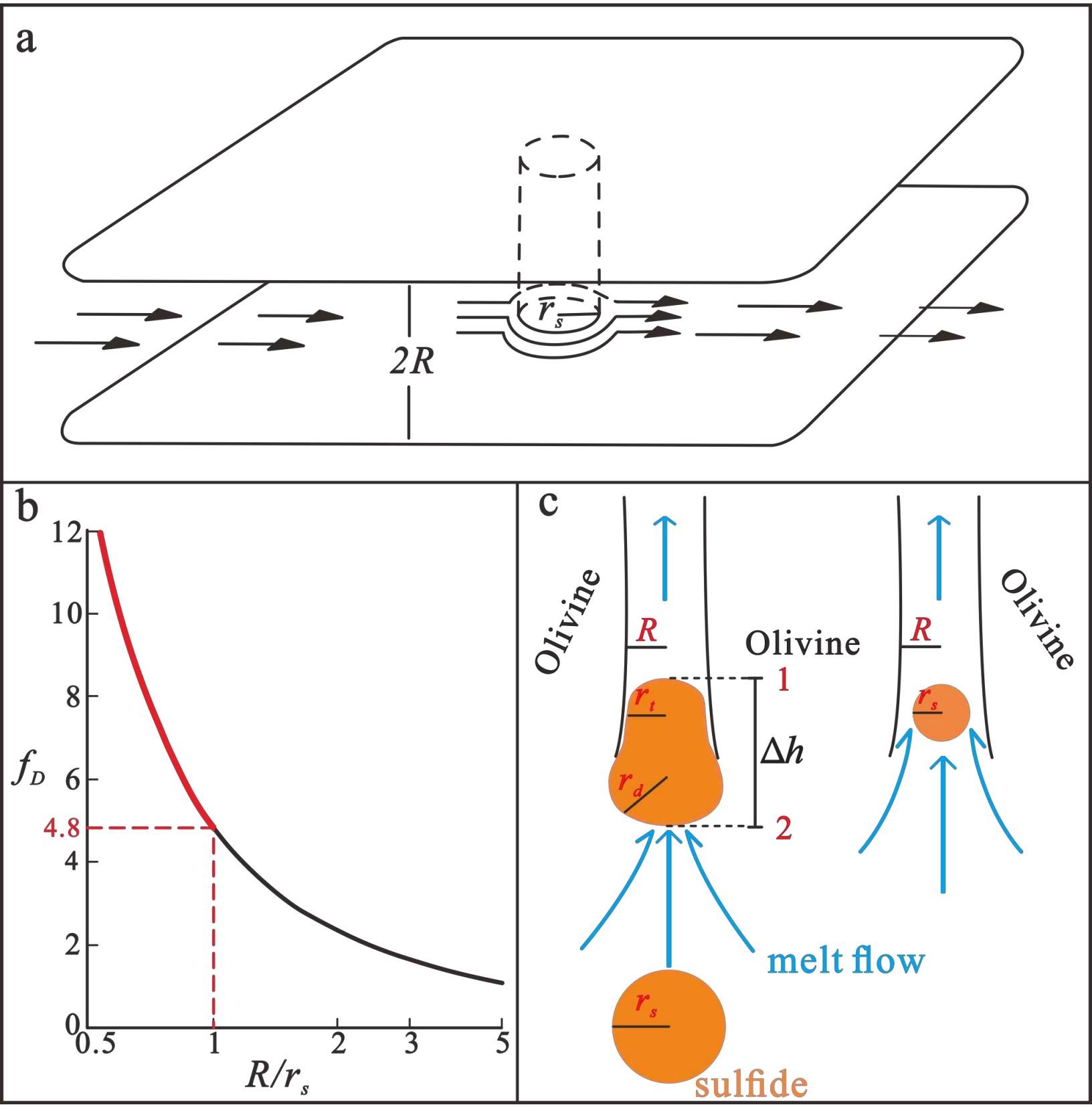
a
r_s
2R
b
12
10
8
f_D
6
4.8
4
2
0
0.5
1
2
3
5
R/r_s
c
Olivine
R
Olivine
1
r_t
Δh
r_d
2
R
Olivine
r_s
melt flow
r_s
sulfide

Figure 11.

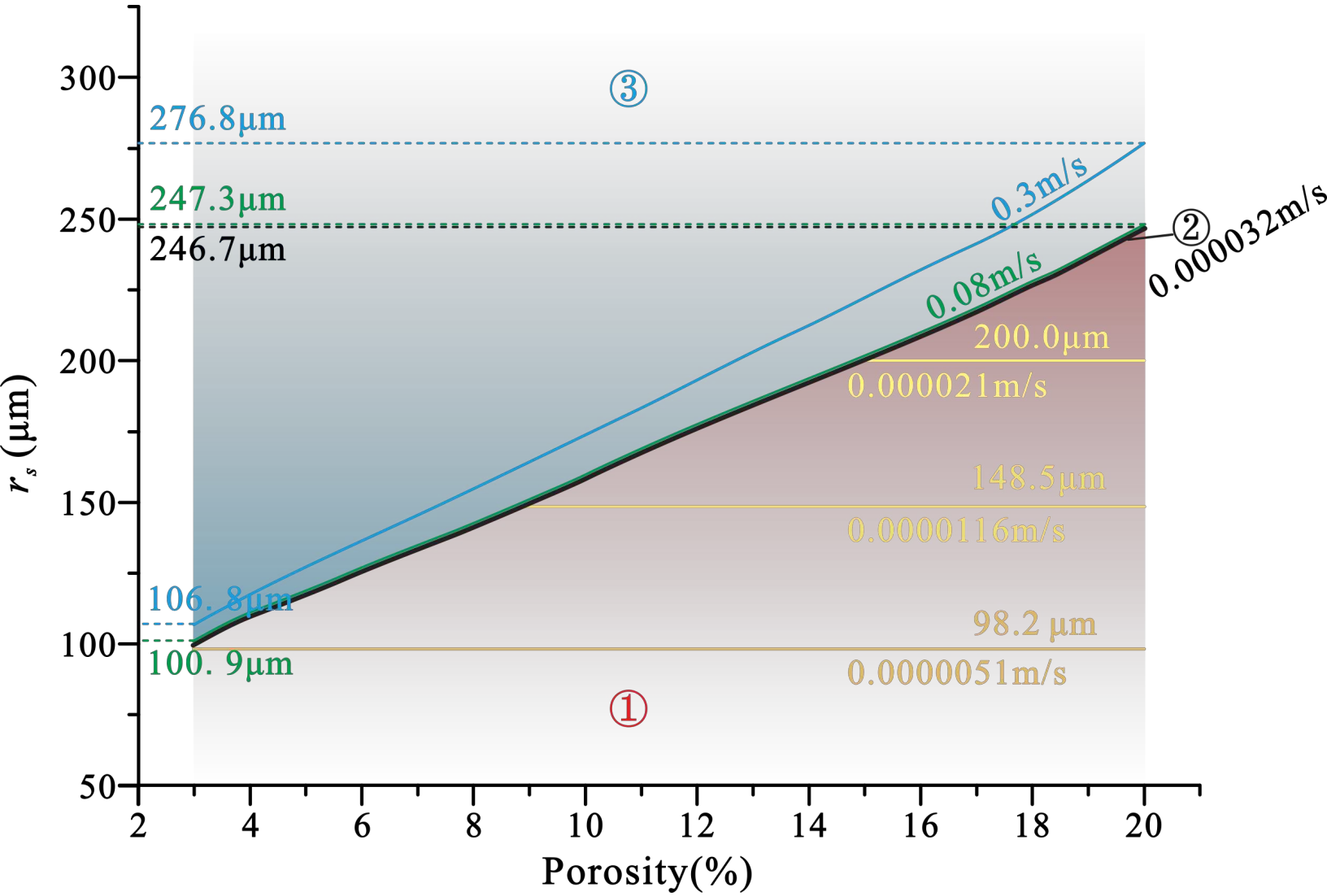
300
250
200
150
100
50
r_s (μm)
2
4
6
8
10
12
14
16
18
20
Porosity(%)
③
①
②
276.8μm
247.3μm
246.7μm
106. 8μm
100. 9μm
0.3m/s
0.08m/s
0.000032m/s
200.0μm
0.000021m/s
148.5μm
0.0000116m/s
98.2 μm
0.0000051m/s

Table 1. Experimental conditions and the observed lithologies

NO.	Starting material (upper peridotite/lower melt source)	Experimental conditions (P/GPa, T/°C, t/h)	Capsule	Litholoties (upper peridotite/reaction interface/melt source)
PC520	Ol+Cpx/ Ol+basalt+sulfide	1.5, 1250, 12	Pt-graphite	Ol+Cpx+SM+SL/ ORL/ Opx+SM+SL
PC527		1.5, 1300, 12		Ol+Cpx+SM+SL/ Ol-SM layer/ ORL/ Opx+SM+SL
PC528		1.5, 1250, 48		Ol+Cpx+SM+SL/ ORL/ Opx+SM+SL
PC537		1.5, 800, 12		Ol+Cpx/ Ol+basalt+sulfide
PC545		1.5, 1250, 72		Ol+Cpx+SM+SL/ Ol-SM layer/ ORL/ Opx+SM+SL
PC548	Ol+Cpx+basalt (5wt.%)/ Ol+basalt+sulfide	1.5, 1250, 48		Ol+Cpx+SM+SL/ ORL/ Opx+SM+SL
PC559		0.5, 1200, 6		Ol+Cpx+SM+SL+V/ Ol+SM+SL
PC560	Ol+Cpx+basalt (5wt.%)/ Ol+basalt+carbonate (2wt.%)+sulfide	1.5, 1250, 24		Ol+Cpx+SM+SL/ Ol-SM layer/ ORL/ Opx+SM+SL

Note: Ol-olivine; Cpx-clinopyroxene; SM-silicate melt; SL-sulfide liquid; V-vapor bubble; ORL-orthopyroxene-rich reaction layer.